INTERNATIONAL JOURNAL FOR NUMERICAL AND ANALYTICAL METHODS IN GEOMECHANICS
Int. J. Numer. Anal. Meth. Geomech. 2008; **32**:1537–1570
Published online 11 February 2008 in Wiley InterScience (www.interscience.wiley.com). DOI: 10.1002/nag.688

Lagrangian meshfree particles method (SPH) for large deformation and failure flows of geomaterial using elastic–plastic soil constitutive model

Ha H. Bui[1,*,†], Ryoichi Fukagawa[1,2], Kazunari Sako[1] and Shintaro Ohno[3]

[1]*Center of Excellence (COE) Promotion Program, Ritsumeikan University, Kusatsu, Shiga, Japan*
[2]*Department of Civil Engineering, Ritsumeikan University, Kusatsu, Shiga, Japan*
[3]*Civil Engineering Design Division, Kajima Corporation, Kusatsu, Shiga, Japan*

SUMMARY

Simulation of large deformation and post-failure of geomaterial in the framework of smoothed particle hydrodynamics (SPH) are presented in this study. The Drucker–Prager model with associated and non-associated plastic flow rules is implemented into the SPH code to describe elastic–plastic soil behavior. In contrast to previous work on SPH for solids, where the hydrostatic pressure is often estimated from density by an *equation of state*, this study proposes to calculate the hydrostatic pressure of soil directly from constitutive models. Results obtained in this paper show that the original SPH method, which has been successfully applied to a vast range of problems, is unable to directly solve elastic–plastic flows of soil because of the so-called SPH tensile instability. This numerical instability may result in unrealistic fracture and particles clustering in SPH simulation. For non-cohesive soil, the instability is not serious and can be completely removed by using a tension cracking treatment from soil constitutive model and thereby give realistic soil behavior. However, the serious tensile instability that is found in SPH application for cohesive soil requires a special treatment to overcome this problem. In this paper, an artificial stress method is applied to remove the SPH numerical instability in cohesive soil. A number of numerical tests are carried out to check the capability of SPH in the current application. Numerical results are then compared with experimental and finite element method solutions. The good agreement obtained from these comparisons suggests that SPH can be extended to general geotechnical problems. Copyright © 2008 John Wiley & Sons, Ltd.

Received 15 February 2007; Revised 24 August 2007; Accepted 11 December 2007

KEY WORDS: smoothed particle hydrodynamics (SPH); failure flows; elastic–plastic model; tensile instability; tension cracking

*Correspondence to: Ha H. Bui, Center of Excellence (COE) Promotion Program, Ritsumeikan University, 1-1-1 Noji-Higashi, Kusatsu, Shiga 525-8577, Japan.
†E-mail: hhbui@fc.ritsumei.ac.jp

1. INTRODUCTION

Problems involving large deformation and post-failure are very important and are active research topics in the field of geomechanics. Numerical predictions of these phenomena could provide useful knowledge for engineering practice and design. In the past few decades, the numerical methods that have most often been used to solve geotechnical problems are the finite element method (FEM) and the discrete element method (DEM). However, dealing with the large deformation and post-failure is generally a difficult task for FEM since this method is a grid-based technique. It thus suffers from grid distortions, which lead to inaccuracies in the solution or even to failure of the computation due to negative values of Jacobian determinants at nodes of numerical integration. DEM simulation does not have that limitation; however, processor power limits this method to small-scale simulation with a few hundred thousand of particles, and it is impossible to handle large-scale problems. In addition, specification of DEM parameters is somewhat ambiguous, and reliable guidelines haven't yet to be clearly established.

Recently, the so-called meshless/meshfree or particle methods have been actively developed and applied to simulate large deformation of continuum or dispersed material. Among these methods, smoothed particle hydrodynamics (SPH) is the longest established and has matured compared with other meshless or particle methods. SPH is a purely Lagrangian meshfree method in which particles carry field variables such as mass, density, stress tensor, etc. and move with the material velocity. Through SPH, the partial differential equations for the continuum are converted into equations of motion of these particles and then solved by updated Lagrangian numerical scheme. Compared with other grid-based numerical methods, SPH has several advantages such as it can handle large deformation and post-failure very well due to its Lagrangian and adaptive nature; complex free surfaces are modeled naturally without any special treatments; complex geometries can be handled without any difficulties and it is relatively easy to incorporate complicated physics.

SPH was originally invented for astrophysical applications [1, 2]. Since its invention, it has been extended and applied to a vast range of applications such as dynamic response of material strength [3–5], free surface fluid flows [6], low-Reynolds number viscous fluid flows [7, 8], incompressible fluid flows [9, 10], heat transfer problems [11], multi-phase flows [12–14], geophysical flows [15, 16] and turbulence flows [17], etc. It was not until 2004 that the first application of SPH for seepage failure flow was attempted by Maeda and Sakai [18], where a power-law nonlinear elastic constitutive model was used to predict the behavior of granular material without considering plastic deformation. Unfortunately, soil behavior is typically more complicated than the nonlinear elastic behavior described in that paper and it is, therefore, commonly believed that such implementations have a limited range of applications. To our knowledge, no application of SPH to solve plastic deformation of soil has yet been reported in the literature. For more information on the SPH method, we refer readers to the textbook by Liu and Liu [19] or the recent review of SPH development by Monaghan [20].

The motivation of this paper is to establish a general SPH framework for solving problems in geomechanics that involve both small and large deformations and to provide a useful numerical tool for geotechnical engineering. For this purpose, extensions of SPH to handle general soil constitutive models with plastic flow rules such as elasto-plastic, elasto-viscous plastic models, etc. are necessary. We present herein, as the first step, an SPH treatment of an elastic–perfectly plastic soil constitutive model wherein the Drucker–Prager model with associated and non-associated plastic flow rules is employed. In contrast to the usual SPH simulation of solid where the hydrostatic pressure is calculated as a function of density change by the SPH '*equation of state*', this paper

DOI: 10.1002/nag

proposes to calculate the hydrostatic pressure of soil (or mean principle stress) directly from the soil constitutive relations. This method provides a general approach to resolve the soil constitutive relations in SPH and therefore gives more realistic and accurate simulation results. In addition, special treatments of solid boundary condition are proposed herein to obtain an accurate stress tensor for soil particles near or on the solid boundary. A further contribution addresses the problem of '*tensile instability*' [21] found in the current SPH application for soil. This instability is almost unrecognizable for non-cohesive soil with small friction angle, but becomes troublesome for relatively high friction angle. The paper shows that, for non-cohesive soil, this numerical instability can be completely removed by using the tension cracking treatment, which thereby allows more realistic prediction of soil behavior in the SPH framework. However, cohesive soil yields a serious tensile instability that requires a special treatment, and in this paper, the artificial stress method [22, 23] with properly selected parameters is used to overcome this numerical instability.

Two main problems have been considered in this study to check the applicability of SPH to soil mechanics. Firstly, SPH is applied to simulate the large deformation and post-failure of non-cohesive and cohesive soils. In particular, gravitational flows of soil are considered. Numerical solutions are then compared with a simple two-dimensional experiment using aluminum bars as a soil model. The method is then validated with a grid-based method, i.e. FEM, through a standard bearing capacity problem in geomechanics. Numerical results obtained from this paper show good agreement with experiment and FEM solutions. Development of shear band during failure, which is generally difficult to simulate by FEM, can also be reproduced clearly through SPH. These results suggest that SPH could be a promising numerical method for future applications in geomechanics. In what follows, the governing equations in SPH are briefly discussed and the presently applied soil constitutive models will be described in the SPH framework. The results of calculations are then presented and discussed.

2. GOVERNING EQUATIONS

The governing equations of soil in the framework of SPH consist of mass and momentum conservation equations as follows:

$$\frac{\mathrm{D}\rho}{\mathrm{D}t} = -\frac{1}{\rho}\frac{\partial v^{\alpha}}{\partial x^{\alpha}} \tag{1}$$

$$\frac{\mathrm{D}v^{\alpha}}{\mathrm{D}t} = \frac{1}{\rho}\frac{\partial \sigma^{\alpha\beta}}{\partial x^{\beta}} + f^{\alpha} \tag{2}$$

where α and β denote the Cartesian components x, y and z with the Einstein convention applied to repeated indices; ρ is the soil density; v is the velocity; $\sigma^{\alpha\beta}$ stands for the total tress tensor of soil, which also corresponds to the effective stress tensor of soil particles described in this paper; f^{α} is the component of acceleration caused by external force, which is the gravity force in this study and $\mathrm{D}/\mathrm{D}t$ is the material derivative, which is defined in a fixed Eulerian frame by

$$\frac{\mathrm{D}}{\mathrm{D}t} = \frac{\partial}{\partial t} + v^{\alpha}\frac{\partial}{\partial x^{\alpha}} \tag{3}$$

It should be noted that the use of the continuity equation in the current SPH application to soil is optional and can be removed from the governing equations if the soil density is kept constant.

DOI: 10.1002/nag

Retaining the continuity equation with the assumption of constant density corresponds to resolving the variation of void ratio or porosity in a soil domain.

To close the system of governing equations (1)–(2), we require a soil constitutive equation for the total stress tensor $\sigma^{\alpha\beta}$. In traditional SPH for a fluid, the total stress tensor is normally divided into two parts: an isotropic hydrostatic pressure p and a deviatoric shear stress s:

$$\sigma^{\alpha\beta} = -p\delta^{\alpha\beta} + s^{\alpha\beta} \tag{4}$$

where $\delta^{\alpha\beta}$ is Kronecker's delta, $\delta^{\alpha\beta}=1$ if $\alpha=\beta$ and $\delta^{\alpha\beta}=0$ if $\alpha\neq\beta$. The hydrostatic pressure p in SPH is normally calculated as a function of density change by an '*equation of state*', whereas the deviatoric shear stress is typically purely viscous and depends on the fluid models. In the SPH application to solid presented by Libersky and Petschek [3] and Libersky *et al.* [4] or more recently by Gray *et al.* [23], such an equation of state was also used. In our work, hydrostatic pressure of soil is instead calculated directly from the soil constitutive equation by the standard definition of mean stress

$$p = -\frac{\sigma^{\gamma\gamma}}{3} = -\frac{1}{3}(\sigma^{xx} + \sigma^{yy} + \sigma^{zz}) \tag{5}$$

where σ^{xx}, σ^{yy} and σ^{zz} are the components of the stress tensor in the x, y and z directions. Throughout this paper, we define that compressive stress corresponds to a negative stress component.

To solve the above system in the SPH framework, one has to approximate these equations using SPH interpolation functions. These procedures will be presented in the next part after some brief descriptions of the soil constitutive models.

3. SOIL CONSTITUTIVE MODELS

3.1. General formulations

As mentioned above, an elastic–perfectly plastic model will be employed in this study to describe the soil behavior. In this section, the general formulation of this model will be briefly presented; details of derivations are given in Appendix A. We start by defining the total strain rate tensor, $\dot{\varepsilon}^{\alpha\beta}$:

$$\dot{\varepsilon}^{\alpha\beta} = \frac{1}{2}\left(\frac{\partial v^{\alpha}}{\partial x^{\beta}} + \frac{\partial v^{\beta}}{\partial x^{\alpha}}\right) \tag{6}$$

For an elastic–perfectly plastic material, $\dot{\varepsilon}^{\alpha\beta}$ is normally composed of two parts: one part of elastic strain rate tensor $\dot{\varepsilon}_{\mathrm{e}}^{\alpha\beta}$ and the other part of plastic strain rate tensor $\dot{\varepsilon}_{\mathrm{p}}^{\alpha\beta}$

$$\dot{\varepsilon}^{\alpha\beta} = \dot{\varepsilon}_{\mathrm{e}}^{\alpha\beta} + \dot{\varepsilon}_{\mathrm{p}}^{\alpha\beta} \tag{7}$$

The elastic strain rate tensor $\dot{\varepsilon}_{\mathrm{e}}^{\alpha\beta}$ is normally calculated by the generalized Hooke's law:

$$\dot{\varepsilon}_{\mathrm{e}}^{\alpha\beta} = \frac{\dot{s}^{\alpha\beta}}{2G} + \frac{1-2v}{3E}\dot{\sigma}^{\gamma\gamma}\delta^{\alpha\beta} \tag{8}$$

DOI: 10.1002/nag

where $\dot{s}^{\alpha\beta}$ is the deviatoric shear stress rate tensor; v is Poisson's ratio; E is Young's modulus; G is the shear modulus and $\dot{\sigma}^{\gamma\gamma}$ is the sum of the three normal stress components, i.e. $\dot{\sigma}^{\gamma\gamma} = \dot{\sigma}^{xx} + \dot{\sigma}^{yy} + \dot{\sigma}^{zz}$.

The plastic strain rate tensor can be computed by using the plastic flow rule

$$\dot{\varepsilon}_{\mathrm{p}}^{\alpha\beta} = \dot{\lambda} \frac{\partial g}{\partial \sigma^{\alpha\beta}} \tag{9}$$

where $\dot{\lambda}$ is the rate of change of the so-called plastic multiplier λ dependent on the state of stress and load history and g is the plastic potential function, which specifies the direction to which the plastic strain develops. If the plastic potential function g is coincident with the yield function f of the material, the flow rule is then called the associated type; otherwise it is called the non-associated type. The plastic multiplier λ has to satisfy the following conditions of the yield criterion:

- $\lambda = 0$ whenever $f < 0$ or $f = 0$ and $\mathrm{d}f < 0$ corresponding to elastic or plastic unloading:
- $\lambda > 0$ whenever $f = 0$ and $\mathrm{d}f = 0$ corresponding to plastic loading.

The value of plastic multiplier λ can be calculated by using the *consistency condition*, which states that

$$\mathrm{d}f = \frac{\partial f}{\partial \sigma^{\alpha\beta}} \mathrm{d}\sigma^{\alpha\beta} = 0 \tag{10}$$

This equation assures that the new stress state $(\sigma^{\alpha\beta} + \mathrm{d}\sigma^{\alpha\beta})$ after loading still satisfies the yield criterion:

$$f(\sigma^{\alpha\beta} + \mathrm{d}\sigma^{\alpha\beta}) = f(\sigma^{\alpha\beta}) + \mathrm{d}f = f(\sigma^{\alpha\beta}) \tag{11}$$

Substituting the elastic and plastic strain rate tensors obtained from Equations (8)–(9) into Equation (7), the total strain rate tensor now can be expressed in the form of stress rate tensor as

$$\dot{\varepsilon}^{\alpha\beta} = \frac{\dot{s}^{\alpha\beta}}{2G} + \frac{1-2v}{3E} \dot{\sigma}^{\gamma\gamma} \delta^{\alpha\beta} + \dot{\lambda} \frac{\partial g}{\partial \sigma^{\alpha\beta}} \tag{12}$$

Using the standard definition of the total stress tensor, $\sigma^{\alpha\beta} = s^{\alpha\beta} + \frac{1}{3}\sigma^{\gamma\gamma}\delta^{\alpha\beta}$, and rearranging Equation (12), the general stress–strain relationship for an elastic–perfectly plastic material can be derived as follows:

$$\dot{\sigma}^{\alpha\beta} = 2G\dot{e}^{\alpha\beta} + K\dot{\varepsilon}^{\gamma\gamma}\delta^{\alpha\beta} - \dot{\lambda}\left[\left(K - \frac{2G}{3}\right)\frac{\partial g}{\partial \sigma^{mn}}\delta^{mn}\delta^{\alpha\beta} + 2G\frac{\partial g}{\partial \sigma^{\alpha\beta}}\right] \tag{13}$$

where α, β are free indexes and m, n are dummy indexes; $\dot{e}^{\alpha\beta} = \dot{\varepsilon}^{\alpha\beta} - \frac{1}{3}\dot{\varepsilon}^{\gamma\gamma}\delta^{\alpha\beta}$ is the deviatoric shear strain rate tensor; K is the elastic bulk modulus, which relates to the shear modulus G and Poisson's ratio v through the following equations:

$$K = \frac{E}{3(1-2v)} \quad \text{and} \quad G = \frac{E}{2(1+v)} \tag{14}$$

DOI: 10.1002/nag

By substituting Equation (13) into the consistency condition (10), the general formulation for the rate of change of plastic multiplier of an elastic–perfectly plastic material can be obtained through

$$\dot{\lambda}=\frac{2G\dot{\varepsilon}^{\alpha\beta}\dfrac{\partial f}{\partial\sigma^{\alpha\beta}}+\left(K-\dfrac{2G}{3}\right)\dot{\varepsilon}^{\gamma\gamma}\dfrac{\partial f}{\partial\sigma^{\alpha\beta}}\delta^{\alpha\beta}}{2G\dfrac{\partial f}{\partial\sigma^{mn}}\dfrac{\partial g}{\partial\sigma^{mn}}+\left(K-\dfrac{2G}{3}\right)\dfrac{\partial f}{\partial\sigma^{mn}}\delta^{mn}\dfrac{\partial g}{\partial\sigma^{mn}}\delta^{mn}} \tag{15}$$

Once the yield function f and the plastic potential function g are substituted for a particular material of interest and total strain rate tensor $\dot{\varepsilon}^{\alpha\beta}$ is prescribed, the rate of change of plastic multiplier can be then determined uniquely. Finally, the stress tensor obtained from Equation (13) is substituted into Equation (2) to close the system of governing equations.

3.2. Drucker–Prager model

The Drucker–Prager yield criterion is chosen in this study to determine the plastic flow regime of soil. This yield condition is expressed through the following equation:

$$f(I_1, J_2)=\sqrt{J_2}+\alpha_\phi I_1-k_c=0 \tag{16}$$

where I_1 and J_2 are, respectively, the first and second invariants of the stress tensor, which are defined by the following equations:

$$I_1=\sigma^{xx}+\sigma^{yy}+\sigma^{zz} \quad \text{and} \quad J_2=\tfrac{1}{2}s^{\alpha\beta}s^{\alpha\beta} \tag{17}$$

α_ϕ and k_c are Drucker–Prager's constants, which related to the Coulomb's material constants c (cohesion) and ϕ (internal friction) in several ways of matching two models as illustrated in Figure 1. Since most of problems described in this paper are in plane strain condition, the Drucker–Prager's constants become

$$\alpha_\phi=\frac{\tan\phi}{\sqrt{9+12\tan^2\phi}} \quad \text{and} \quad k_c=\frac{3c}{\sqrt{9+12\tan^2\phi}} \tag{18}$$

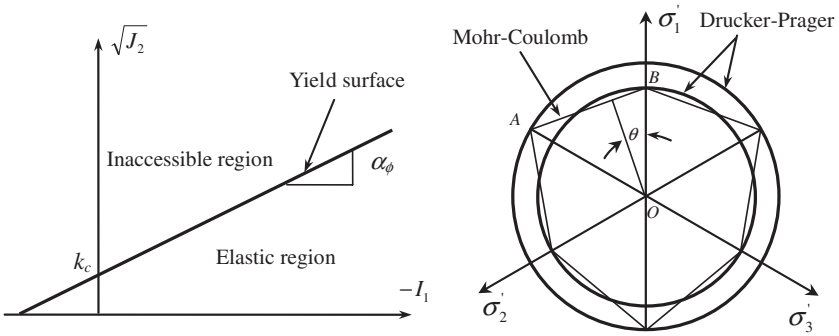

Figure 1. Drucker–Prager yield criterion.

DOI: 10.1002/nag

In addition to the yield criterion, the plastic potential function also has to be determined to completely specify the stress–strain relationship. In this paper, two types of plastic flow rules are implemented into the SPH code. The first one is the associated plastic flow rule, which indicates that the plastic potential function of the Drucker–Prager material has the same form with the yield criterion, namely,

$$g = \sqrt{J_2} + \alpha_\phi I_1 - k_c \tag{19}$$

The second one is the non-associated flow rule, in which the plastic potential function has the following form:

$$g = \sqrt{J_2} + 3I_1 \sin\psi \tag{20}$$

where ψ is the dilatancy angle, which is assumed to be zero in this paper. A zero dilatancy angle of the non-associated flow rule indicates that the material is plastically incompressible.

Substituting Equation (19) into Equations (13)–(15), see Appendix for details, the final stress–strain relationship of the Drucker–Prager elastic–perfectly plastic soil model with associated flow rule can be expressed as

$$\dot{\sigma}^{\alpha\beta} = 2G\dot{e}^{\alpha\beta} + K\dot{\varepsilon}^{\gamma\gamma}\delta^{\alpha\beta} - \dot{\lambda}\left[3\alpha_\phi K\delta^{\alpha\beta} + \frac{G}{\sqrt{J_2}}s^{\alpha\beta}\right] \tag{21}$$

where the rate of change of plastic multiplier $\dot{\lambda}$ is estimated for this soil model from the following equation:

$$\dot{\lambda} = \frac{3\alpha_\phi K\dot{\varepsilon}^{\gamma\gamma} + (G/\sqrt{J_2})s^{\alpha\beta}\dot{\varepsilon}^{\alpha\beta}}{9\alpha_\phi^2 K + G} \tag{22}$$

Similarly, the stress–strain relationship of the non-associated flow rule can also be derived by substituting Equation (20) into Equations (13)–(15) leading to

$$\dot{\sigma}^{\alpha\beta} = 2G\dot{e}^{\alpha\beta} + K\dot{\varepsilon}^{\gamma\gamma}\delta^{\alpha\beta} - \dot{\lambda}\left[9K\sin\psi\delta^{\alpha\beta} + \frac{G}{\sqrt{J_2}}s^{\alpha\beta}\right] \tag{23}$$

with the following equation for the rate of change of plastic multiplier $\dot{\lambda}$:

$$\dot{\lambda} = \frac{3\alpha K\dot{\varepsilon}^{\gamma\gamma} + (G/\sqrt{J_2})s^{\alpha\beta}\dot{\varepsilon}^{\alpha\beta}}{27\alpha_\phi K\sin\psi + G} \tag{24}$$

From the above stress–strain relationships, it can be seen that the main difference between these two models lies in the effect of dilatancy. Dilatancy always takes part in the associated flow rule soil model, whereas this contribution to the non-associated flow rule is optional through the choice of dilatancy angle ψ. For the granular materials described in this paper, the non-associated flow rule soil model is adopted with zero dilatancy angle. In the SPH framework, Equations (21)–(24) can be solved directly using the updated Lagrangian formulation rather than building a stiffness matrix as in a FEM simulation.

DOI: 10.1002/nag

When considering a large deformation problem, a stress rate that is invariant with respect to rigid-body rotation must be employed for the constitutive relations. In this study, the Jaumann stress rate, $\dot{\hat{\sigma}}^{\alpha\beta}$ is adopted:

$$\dot{\hat{\sigma}}^{\alpha\beta} = \dot{\sigma}^{\alpha\beta} - \sigma^{\alpha\gamma}\dot{\omega}^{\beta\gamma} - \sigma^{\gamma\beta}\dot{\omega}^{\alpha\gamma} \tag{25}$$

where $\dot{\omega}$ is spin rate tensor defined as

$$\dot{\omega}^{\alpha\beta} = \frac{1}{2}\left(\frac{\partial v^{\alpha}}{\partial x^{\beta}} - \frac{\partial v^{\beta}}{\partial x^{\alpha}}\right) \tag{26}$$

As a result, the final form of stress–strain relationships for the associated and non-associated flow rules soil models are, respectively, modified to

$$\dot{\sigma}^{\alpha\beta} - \sigma^{\alpha\gamma}\dot{\omega}^{\beta\gamma} - \sigma^{\gamma\beta}\dot{\omega}^{\alpha\gamma} = 2G\dot{e}^{\alpha\beta} + K\dot{\varepsilon}^{\gamma\gamma}\delta^{\alpha\beta} - \dot{\lambda}\left[3\alpha_{\phi}K\delta^{\alpha\beta} + \frac{G}{\sqrt{J_2}}s^{\alpha\beta}\right] \tag{27}$$

$$\dot{\sigma}^{\alpha\beta} - \sigma^{\alpha\gamma}\dot{\omega}^{\beta\gamma} - \sigma^{\gamma\beta}\dot{\omega}^{\alpha\gamma} = 2G\dot{e}^{\alpha\beta} + K\dot{\varepsilon}^{\gamma\gamma}\delta^{\alpha\beta} - \dot{\lambda}\left[9K\sin\psi\delta^{\alpha\beta} + \frac{G}{\sqrt{J_2}}s^{\alpha\beta}\right] \tag{28}$$

where the rate of change of plastic multipliers $\dot{\lambda}$ are still calculated by Equations (22) and (24). In order to solve the above constitutive relations, i.e. Equations (27) and (28), we have to first discretize these equations into the SPH framework for every particle and then interpolate them by the updated Lagrangian formulation. In fact, in the case of very large deformation the above constitutive relations are not incrementally objective, which means that it does not preserve exactly the objectivity of the stress and strain measures for finite time increments, although the objective measure of the Jaummann stress rate is used. This is because this paper adopted small deformation theory for the constitutive relations. Full incremental objectivity can be achieved by applying the finite deformation formulations to the constitutive relations (see Chen and Mizuno [24] and papers cited therein for details). In this study, the inaccuracy caused by the lack of incremental objectivity is not significant as a very small time step is applied in the explicitly updated Lagrangian procedure for solving the dynamic equations. The above soil constitutive model requires three soil parameters: cohesion coefficient (c), friction angle (ϕ) and elastic bulk modulus (K), which can be specified from shear box test or triaxial test.

3.3. Numerical errors in computational plasticity

As the elastic–perfectly plastic soil constitutive model was adopted in this study, the behavior of soil must be consistent with this model i.e. the stress state must not lie outside the yield surface when plastic deformation takes place. However, due to numerical errors during computation, which are commonly found in computational plasticity, the stress state of soil may leave the elastic domain. In such a circumstance, a return mapping algorithm is often used to numerically return the stress state to the yield surface. In the current SPH applications for elasto-plastic material, the same problem occurs. Therefore, the following procedure [24] will be used for the return mapping algorithm.

DOI: 10.1002/nag

3.3.1. Tension cracking treatment. If, during computation, the stress state of soil moves beyond the apex of the yield surface, e.g. to the stress state at point F illustrated in Figure 2, numerical error occurs. This error is the so-called tension cracking, which was described by Chen and Mizuno [24] in their implementation of a FEM code. In our work, the same tension cracking problem is also found. In fact, this problem is similar to the so-called SPH tensile instability [21], which may result in unrealistic fracture or particles forming clumps in SPH simulation when the material is in tension. Computationally, to remove this tension cracking, it is necessary to shift the hydrostatic stress component to the apex of the yield surface. Following Chen and Mizuno [24], if the stress state of material at a time step n exceeds the apex of the yield surface, which satisfies the following condition:

$$-\alpha_\phi I_1^n + k_c < 0 \tag{29}$$

we shall adjust the normal stress components to new values $\tilde{\sigma}$ so that the hydrostatic pressure corresponds to that at the apex (see Figure 2) according to the following equations:

$$\tilde{\sigma}_n^{xx} = \sigma_n^{xx} - \frac{1}{3}\left(I_1^n - \frac{k_c}{\alpha_\phi}\right) \tag{30a}$$

$$\tilde{\sigma}_n^{yy} = \sigma_n^{yy} - \frac{1}{3}\left(I_1^n - \frac{k_c}{\alpha_\phi}\right) \tag{30b}$$

$$\tilde{\sigma}_n^{zz} = \sigma_n^{zz} - \frac{1}{3}\left(I_1^n - \frac{k_c}{\alpha_\phi}\right) \tag{30c}$$

while the shearing stresses $\sigma_n^{xy}, \sigma_n^{xz}$, and σ_n^{yz} remain unchanged. In this paper, we will show that the above tension cracking treatment not only removes the numerical error in computational plasticity but also solves the SPH tensile instability problem in non-cohesive soil. However, the same approach is unable to remove tensile instability in cohesive soil since the apex of the yield surface of this material is located in the tensile stress region ($I_1 > 0$). To remove this numerical instability for cohesive soil, the artificial stress method [22, 23] will be applied.

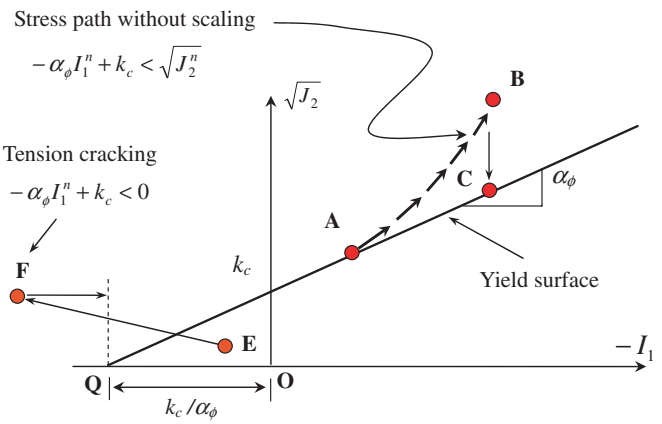

Figure 2. Stress states in tension cracking (E⇒F) and imperfectly plastic (A⇒B) responses.

DOI: 10.1002/nag

3.3.2. Stress-scaling back procedure. When an elastic–perfectly plastic material experiences plastic deformation, the stress state must always lie on the yield surface during plastic loading. However, errors in computation may result in a stress state that lies far away from the yield surface, e.g. the path *AB* in Figure 2. In such a circumstance, a stress-rescaling procedure should be employed to return the stress state to the yield surface. This process is given in the following: A schematic stress path associated with this stress-rescaling procedure is shown in Figure 2 as the arrow line from B to C. To scale the stress state at B back to the corresponding state at C on the yield surface, a scaling factor r is introduced. For the Drucker–Prager yield criterion, this scaling factor at time step n is defined by

$$r^n = \frac{-\alpha_\phi I_1^n + k_c}{\sqrt{J_2^n}} \tag{31}$$

Accordingly, when the stress state of soil exceeds the yield surface, which corresponds, for the Drucker–Prager yield criterion, to the following condition:

$$-\alpha_\phi I_1^n + k_c < \sqrt{J_2^n} \tag{32}$$

the deviatoric shear stress components are reduced in proportion to the scaling factor r, whereas the hydrostatic stress component I_1 is left unchanged, according to the following relations:

$$\tilde{\sigma}_n^{xx} = r^n s_n^{xx} + \tfrac{1}{3} I_1^n \tag{33a}$$

$$\tilde{\sigma}_n^{yy} = r^n s_n^{yy} + \tfrac{1}{3} I_1^n \tag{33b}$$

$$\tilde{\sigma}_n^{zz} = r^n s_n^{zz} + \tfrac{1}{3} I_1^n \tag{33c}$$

$$\tilde{\sigma}_n^{xy} = r^n s_n^{xy} \tag{33d}$$

$$\tilde{\sigma}_n^{xz} = r^n s_n^{xz} \tag{33e}$$

$$\tilde{\sigma}_n^{yz} = r^n s_n^{yz} \tag{33f}$$

where

$$I_1^n = \sigma_n^{xx} + \sigma_n^{yy} + \sigma_n^{zz} \tag{33g}$$

Since this work uses the leapfrog (LF) algorithm for numerical integration, as described in Section 4.6, the stress of soil is also interpolated at the half-time step $(n+\frac{1}{2})$. For consistency, the above return mapping algorithm is applied at the half-time step by using exactly the above procedure.

4. SPH FORMULATIONS

4.1. SPH concepts and discretization of governing equations

In the SPH method, the computational domain is discretized into a finite number of particles (or points). These particles carry material properties such as velocity, density, stress, etc. and move with the material velocity according to the governing equations (1)–(2). The material properties of

DOI: 10.1002/nag

each particle are then calculated through the use of an interpolation process over its neighboring particles. The interpolation process is based on the integral representation of a field function $f(\mathbf{x})$ as follows:

$$\langle f(\mathbf{x})\rangle = \int_{\Omega} f(\mathbf{x}')W(\mathbf{x}-\mathbf{x}', h)\,\mathrm{d}\mathbf{x}' \tag{34}$$

where W is the kernel or smoothing function and h is the smoothing length, which defines the influence domain of W. The smoothing function W must be chosen to satisfy three conditions. The first one is called *the normalization condition*

$$\int_{\Omega} W(\mathbf{x}-\mathbf{x}', h)\,\mathrm{d}\mathbf{x}' = 1 \tag{35}$$

The second condition is *the delta function property* that should be satisfied when the smoothing length approaches zero:

$$\lim_{h\to 0} W(\mathbf{x}-\mathbf{x}', h) = \delta(\mathbf{x}-\mathbf{x}') \tag{36}$$

Last is *the compact support condition*:

$$W(\mathbf{x}-\mathbf{x}', h) = 0 \quad \text{when } |\mathbf{x}-\mathbf{x}'| > kh \tag{37}$$

where k is a constant, which specifies the non-zero region of the smoothing function for a point at position vector $\mathbf{x}$. This effective area is called the support domain for the smoothing function of point $\mathbf{x}$. From the compact support condition (37), integration over the entire problem domain Ω is localized to integration over the support domain of the smoothing function. Therefore, the integration domain Ω is usually the same as the support domain. From the above equations (34)–(37), if the smoothing function W is an even function with respect to $\mathbf{x}$, by using the Taylor series expansion of $f(\mathbf{x}')$ around $\mathbf{x}$, it can be shown that the integral representation of $f(\mathbf{x})$ is of second-order accuracy (h^2).

The choice of smoothing function in SPH will directly affect the accuracy, efficiency and the stability of numerical algorithm. A number of smoothing functions have been proposed in the SPH literature, ranging from Gaussian to cubic spline functions with a compact support condition. We apply herein the most popular cubic spline function, proposed by Monaghan and Lattanzio [25], which has the following form:

$$W_{ij} = \alpha_d \times \begin{cases} \frac{2}{3} - q^2 + \frac{1}{2}q^3, & 0 \leqslant q < 1 \\ \frac{1}{6}(2-q)^3, & 1 \leqslant q < 2 \\ 0, & q \geqslant 2 \end{cases} \tag{38}$$

where α_d is the normalization factor, which is $15/(7\pi h^2)$ in two-dimensional space and q is the normalized distance between particles i and j defined as $q = r/h$. For this cubic spline function, the parameter k, which defines the effective area of support domain, is 2.

The continuous integral representation (34) can be now discretized as a summation over the particles in the support domain as follows:

$$\langle f(\mathbf{x})\rangle \approx \sum_{j=1}^{N} \frac{m_j}{\rho_j} f(\mathbf{x}_j)W(\mathbf{x}-\mathbf{x}_j, h) \tag{39}$$

DOI: 10.1002/nag

where $j=1,2,\ldots,N$ indicate particles within the support domain of the particle at $\mathbf{x}$, the so-called neighboring; m_j and ρ_j are, respectively, the mass and the density of particle j (m_j/ρ_j gives the volume V_j of particle j).

The approximation for the spatial derivative $\partial f(\mathbf{x})/\partial\mathbf{x}$ can be obtained simply by substituting $f(\mathbf{x})$ with $\partial f(\mathbf{x})/\partial\mathbf{x}$ in Equation (34). Integrating by parts and using the divergence theorem, one obtains

$$\left\langle \frac{\partial f(\mathbf{x})}{\partial \mathbf{x}} \right\rangle = \int_S f(\mathbf{x}')W(\mathbf{x}-\mathbf{x}',h)\cdot\mathbf{n}\,\mathrm{d}S - \int_\Omega f(\mathbf{x}')\frac{\partial W(\mathbf{x}-\mathbf{x}',h)}{\partial \mathbf{x}'}\,\mathrm{d}\mathbf{x}' \tag{40}$$

where $\mathbf{n}$ is the unit vector normal to the surface S. Since the smoothing function W is defined to have compact support, the surface integral in the right-hand side of Equation (40) is identically zero. Therefore, using the summation approach to approximate the continuous integral as was done in deriving Equation (39), the approximation of spatial derivative of a function $f(\mathbf{x})$ can be obtained by

$$\left\langle \frac{\partial f(\mathbf{x})}{\partial \mathbf{x}} \right\rangle \approx -\sum_{j=1}^{N}\frac{m_j}{\rho_j}f(\mathbf{x}_j)\cdot\frac{\partial W(\mathbf{x}-\mathbf{x}_j,h)}{\partial \mathbf{x}_j} \tag{41}$$

From Equations (39) and (41), the particle approximation for a function and its spatial derivatives at a particle i can finally be expressed in condensed form as

$$f(\mathbf{x}_i) = \sum_{j=1}^{N}\frac{m_j}{\rho_j}f(\mathbf{x}_j)W_{ij} \tag{42}$$

$$\frac{\partial f(\mathbf{x}_i)}{\partial \mathbf{x}} = \sum_{j=1}^{N}\frac{m_j}{\rho_j}f(\mathbf{x}_j)\cdot\frac{\partial W_{ij}}{\partial \mathbf{x}_i} \tag{43}$$

where

$$W_{ij} = W(\mathbf{x}_i-\mathbf{x}_j,h) \quad \text{and} \quad \frac{\partial W_{ij}}{\partial \mathbf{x}_i} = \left(\frac{\mathbf{x}_i-\mathbf{x}_j}{r}\right)\frac{\partial W_{ij}}{\partial r} \tag{44}$$

with r is the relative distance between particles i and j and it is defined as $r=|\mathbf{x}_i-\mathbf{x}_j|$. The minus sign in Equation (41) no longer appears in Equation (43) since the gradient $\partial W_{ij}/\partial\mathbf{x}_i$ is taken with respect to the $\mathbf{x}_i$ rather than $\mathbf{x}_j$.

Now, it is possible to approximate the velocity gradient of a particle i by directly applying Equation (43) leading to

$$\frac{\partial v_i^\alpha}{\partial x^\beta} = \sum_{j=1}^{N}\frac{m_j}{\rho_j}v_j^\alpha\cdot\frac{\partial W_{ij}}{\partial x_i^\beta} \tag{45}$$

In practice, however, it is more accurate to involve the velocity difference between two interacting particles rather than using a single velocity of neighboring particle. This can be obtained by applying (43) to evaluate the gradient of the unity:

$$\frac{\partial 1}{\partial x^\beta} = \sum_{j=1}^{N}\frac{m_j}{\rho_j}\frac{\partial W_{ij}}{\partial x_i^\beta} = 0 \tag{46}$$

DOI: 10.1002/nag

then adding this sum (46), as multiplied by the velocity $(-v_i^\alpha)$, to the right-hand side of (45) leading to

$$\frac{\partial v_i^\alpha}{\partial x^\beta} = \sum_{j=1}^{N} \frac{m_j}{\rho_j} (v_j^\alpha - v_i^\alpha) \cdot \frac{\partial W_{ij}}{\partial x_i^\beta} \tag{47}$$

Approximation (47) ensures that the gradients of a constant velocity field vanish.

The SPH approximation of mass and momentum conservation equations is now straightforward by applying Equations (42)–(44) to Equations (1)–(2). However, different transformations or operations may result in different discretized form of SPH equations. In what follows, we will present the most commonly used formulations in the current SPH literature. First, the right-hand side of the density continuity equation can be rewritten as

$$-\rho \frac{\partial v^\alpha}{\partial x^\alpha} = -\left(\frac{\partial (\rho v^\alpha)}{\partial x^\alpha} - v^\alpha \frac{\partial \rho}{\partial x^\alpha} \right) \tag{48}$$

Then by applying the SPH approximation (43) to the gradient terms in (48) and evaluating the velocity in the last term of (48) at particle i, the SPH formulation for density evaluation can be obtained by

$$\frac{\mathrm{D}\rho_i}{\mathrm{D}t} = \sum_{j=1}^{N} m_j (v_i^\alpha - v_j^\alpha) \cdot \frac{\partial W_{ij}}{\partial x_i^\alpha} \tag{49}$$

Considering the momentum equation (2), the right-hand side of this equation can be also rewritten in the following form:

$$\frac{1}{\rho} \frac{\partial \sigma^{\alpha\beta}}{\partial x^\beta} = \frac{\partial}{\partial x^\beta} \left(\frac{\sigma^{\alpha\beta}}{\rho} \right) + \frac{\sigma^{\alpha\beta}}{\rho^2} \frac{\partial \rho}{\partial x^\beta} \tag{50}$$

using the same approach as was done to approximate the density for Equation (50), the most popular SPH approximation form for the momentum equation can be derived as follows:

$$\frac{\mathrm{D}v_i^\alpha}{\mathrm{D}t} = \sum_{j=1}^{N} m_j \left(\frac{\sigma_i^{\alpha\beta}}{\rho_i^2} + \frac{\sigma_j^{\alpha\beta}}{\rho_j^2} \right) \frac{\partial W_{ij}}{\partial x^\beta} + g^\alpha \tag{51}$$

Discretizations of soil constitutive equations in the SPH framework are also straightforward. The stress–strain relationship (27) for the associated flow rule soil model of a given particle i in the SPH formulation can be immediately expressed as follows:

$$\frac{\mathrm{D}\sigma_i^{\alpha\beta}}{\mathrm{D}t} = \sigma_i^{\alpha\gamma} \dot{\omega}_i^{\beta\gamma} + \sigma_i^{\gamma\beta} \dot{\omega}_i^{\alpha\gamma} + 2G\dot{e}_i^{\alpha\beta} + K\dot{\varepsilon}_i^{\gamma\gamma} \delta_i^{\alpha\beta} - \dot{\lambda}_i \left[3\alpha_\phi K \delta^{\alpha\beta} + \frac{G}{\sqrt{J_2}} s_i^{\alpha\beta} \right] \tag{52}$$

where the rate of change of plastic multiplier $\dot{\lambda}_i$ for particle i is expressed in the SPH formulation using Equation (22), leading to

$$\dot{\lambda}_i = \frac{3\alpha_\phi K \dot{\varepsilon}_i^{\gamma\gamma} + (G/\sqrt{J_2}) s_i^{\alpha\beta} \dot{\varepsilon}_i^{\alpha\beta}}{9\alpha_\phi^2 K + G} \tag{53}$$

DOI: 10.1002/nag

The same rule used to derive Equations (52) and (53) is applied to obtain the SPH formulation of stress–strain relationship for the non-associated flow rule soil model. Equation (23) in SPH form is, accordingly, immediately expressed as

$$\frac{\mathrm{D}\sigma_i^{\alpha\beta}}{\mathrm{D}t}=\sigma_i^{\alpha\gamma}\dot{\omega}_i^{\beta\gamma}+\sigma_i^{\gamma\beta}\dot{\omega}_i^{\alpha\gamma}+2G\dot{e}_i^{\alpha\beta}+K\dot{\varepsilon}_i^{\gamma\gamma}\delta_i^{\alpha\beta}-\dot{\lambda}_i\left[9K\sin\psi\delta^{\alpha\beta}+\frac{G}{\sqrt{J_2}}s_i^{\alpha\beta}\right] \tag{54}$$

with the rate of change of plastic multiplier $\dot{\lambda}_i$ for non-associated type specified by

$$\dot{\lambda}_i=\frac{3\alpha_\phi K\dot{\varepsilon}_i^{\gamma\gamma}+(G/\sqrt{J_2})s_i^{\alpha\beta}\dot{\varepsilon}_i^{\alpha\beta}}{27\alpha_\phi K\sin\psi+G} \tag{55}$$

To complete the above soil constitutive equations, the strain and spin rate tensors of a particle also have to be discretized into the SPH formulations. These are obtained by substituting Equation (47) into Equations (6) and (26) leading to

$$\dot{\varepsilon}^{\alpha\beta}=\frac{1}{2}\left(\frac{\partial v^\alpha}{\partial x^\beta}+\frac{\partial v^\beta}{\partial x^\alpha}\right)=\frac{1}{2}\left[\sum_{j=1}^{N}\frac{m_j}{\rho_j}(v_j^\alpha-v_i^\alpha)\frac{\partial W_{ij}}{\partial x_i^\beta}+\sum_{j=1}^{N}\frac{m_j}{\rho_j}(v_j^\beta-v_i^\beta)\frac{\partial W_{ij}}{\partial x_i^\alpha}\right] \tag{56}$$

$$\dot{\omega}^{\alpha\beta}=\frac{1}{2}\left(\frac{\partial v^\alpha}{\partial x^\beta}-\frac{\partial v^\beta}{\partial x^\alpha}\right)=\frac{1}{2}\left[\sum_{j=1}^{N}\frac{m_j}{\rho_j}(v_j^\alpha-v_i^\alpha)\frac{\partial W_{ij}}{\partial x_i^\beta}-\sum_{j=1}^{N}\frac{m_j}{\rho_j}(v_j^\beta-v_i^\beta)\frac{\partial W_{ij}}{\partial x_i^\alpha}\right] \tag{57}$$

Finally, the particle positions in SPH are moved according to the following integration:

$$\frac{\mathrm{d}x_i^\alpha}{\mathrm{d}t}=v_i^\alpha \tag{58}$$

4.2. Artificial viscosity

It has often been observed that numerical solutions present large unphysical oscillations and are unstable if a dissipative term is not introduced into the governing equations. This is because shocks are always present, mostly in the first stages when initial conditions must relax, and if they are not smeared out over a length scale sufficiently larger than the discretization step h, strong instability can occur. To improve the numerical stability and to damp out such undesirable oscillations, a dissipative term Π_{ij} (or artificial viscosity) is introduced into the pressure term of the momentum equation. The artificial viscosity is incorporated into the momentum equation (51) in the following way:

$$\frac{\mathrm{D}v_i^\alpha}{\mathrm{D}t}=\sum_{j=1}^{N}m_j\left(\frac{\sigma_i^{\alpha\beta}}{\rho_i^2}+\frac{\sigma_j^{\alpha\beta}}{\rho_j^2}-\Pi_{ij}\delta^{\alpha\beta}\right)\frac{\partial W_{ij}}{\partial x^\beta}+g^\alpha \tag{59}$$

Many numerical tests have proved the advantage of this term in improving numerical stability and removing the penetration between particles. Of several proposals for artificial viscosity developed so far, the most widely applied is that derived by Monaghan [26]:

$$\Pi_{ij}=\begin{cases}\dfrac{-\alpha_\Pi c_{ij}\phi_{ij}+\beta_\Pi\phi^2}{\rho_{ij}}, & v_{ij}\cdot x_{ij}<0\\ 0, & v_{ij}\cdot x_{ij}\geqslant 0\end{cases} \tag{60}$$

DOI: 10.1002/nag

where

$$\phi_{ij} = \frac{h_{ij} v_{ij} \cdot x_{ij}}{|x_{ij}|^2 + 0.01 h_{ij}^2}, \quad c_{ij} = \frac{c_i + c_j}{2}, \quad \rho_{ij} = \frac{\rho_i + \rho_j}{2} \tag{61}$$

$$h_{ij} = \tfrac{1}{2}(h_i + h_j), \quad x_{ij} = x_i - x_j, \quad v_{ij} = v_i - v_j \tag{62}$$

In the above equation, α_Π and β_Π are constants; c is the sound speed in soil, which typically lies in the range 450–600 m/s [27, 28] and $0.01h_{ij}^2$ is used to prevent numerical divergence when two particles approach each other. In this study, the maximum sound speed $c = 600\,\text{m/s}$ is applied for the artificial viscosity, although a smaller value can be used [6].

The artificial viscosity actually consists of two contributions: one is linearly proportional to the divergence of velocity, which produces a shear and bulk viscosity [26] and another one, which is quadratic in the velocity divergence, is substantially analogous to the Von Neumann–Richtmyer viscosity and able to handle high Mach number flows. According to Monaghan [26], this artificial viscosity has a number of desirable features:

1. It is Galilean invariant.
2. It vanishes for rigid-body rotation.
3. It conserves total linear and angular momenta.

The values of α_Π and β_Π should be chosen according to particular applications. Monaghan [6] chose $\alpha_\Pi = 0.01$ and $\beta_\Pi = 0$ for his first implementation of SPH for quasi-incompressible free surface flow; Libersky *et al.* [4] chose $\alpha_\Pi = 2.5$ and $\beta_\Pi = 2.5$ for SPH simulation of solid, etc. In most cases, Monaghan suggests choosing these values close to 1 for best results. The main drawback of this approach is that it introduces a shear viscosity, or dissipation of energy, into the flows when a large value of α_Π is used. Most computations described herein are assigned with $\alpha_\Pi = 0.1$ and $\beta_\Pi = 0.1$. The second term, associated with β_Π, does not have much effect in the present study since the velocity of particles is small compared with the sound speed. Our tests give similar results for the value of β_Π between 0 and 2.5. It is also worth noting that the artificial viscosity can also be determined 'dynamically' [29] by setting the α_Π as a functions of time and space, which allows rather large values where necessary to suppress large unphysical oscillations and decay in quiescent regions where it is unnecessary. However, this technique is not necessary in this study; we only chose value of α_Π appropriate for numerical stability.

4.3. Tensile instability and artificial stress method

When SPH is applied to solids, the SPH particles mimic the behavior of the atoms. If the solid is compressed, the atoms repel each other. On the other hand, if it expands, the atoms attract each other. SPH particles behave the same way except that, when material is stretched, the attraction can result in the SPH particles forming clumps. This instability was first studied in detail by Swegle *et al.* [21], who related it to the sign of the pressure and the sign of the second derivative of the interpolating kernel. It is commonly called the *tensile instability*. There have been a number of attempts to remove this numerical instability by different approaches [30–35], but the most effective and successful has been the method proposed recently by Monaghan [22] and Gray *et al.* [23]. The key idea of this method is to introduce a small repulsive force between neighboring particles that mimics interatomic repulsion and prevents them from getting closer when in a state of tensile stress and thereby subject to attraction due to the original SPH formulation. This repulsive force,

DOI: 10.1002/nag

according to Monaghan [22], must increase as the separation between two particles decreases. In this paper, we will show that a slight tensile instability problem will occur for non-cohesive soil and for high friction angle although not for small friction angle. We then demonstrate that the tensile instability in non-cohesive soil can be completely removed by the tension cracking treatment that was described in Section 3.3.1. However, this approach is not sufficient to remove the serious tensile instability problem that is found in SPH applied to cohesive soil. In such circumstances, the artificial stress method [22, 23] is implemented. To do so, we replace the expression (59) with

$$\frac{\mathrm{D}v_i^\alpha}{\mathrm{D}t} = \sum_{j=1}^{N} m_j \left(\frac{\sigma_i^{\alpha\beta}}{\rho_i^2} + \frac{\sigma_j^{\alpha\beta}}{\rho_j^2} - \Pi_{ij}\delta^{\alpha\beta} + f_{ij}^n (R_i^{\alpha\beta} + R_j^{\alpha\beta}) \right) \frac{\partial W_{ij}}{\partial x^\beta} + g^\alpha \tag{63}$$

where n is the exponent dependent on the smoothing kernel and is chosen according to the analysis of dispersion equations [22, 23]; f_{ij} is the repulsive force term and is specified, according to Monaghan [22], in terms of the kernels:

$$f_{ij} = \frac{W_{ij}}{W(\Delta d, h)} \tag{64}$$

where Δd is the initial particle spacing. In this paper, h is assumed to be constant so that $W(\Delta d, h)$ is also constant. For the cubic spline kernel, the ratio $W(0,h)/W(\Delta d, h)$ has the value 4 if h equals Δd; if $h = 1.2\Delta d$ (the typical h used in this paper), the ratio is about 2.55. For problems described herein, the exponent n is chosen to be 2.55, although Gray *et al.* [23] suggested to choose $n = 4$ for best solutions. With $h = 1.2\Delta d$, the repulsive force term will increase by a factor of about 11 as r_{ij} decreases from Δd to zero, whereas this force decreases rapidly according to $(r_{ij} - 2h)^{3n}$ in the domain $h \leqslant r_{ij} \leqslant 2h$. This ensures that the effect of the artificial stress is confined to nearest neighboring particles. In practice, the smoothing length in SPH simulation may be varied according to the distribution of particles [19, 26]. In such a circumstance, it is also possible to vary n accordingly [36]. It is worth pointing out that this artificial stress only takes effect when particles clump (i.e. $r_{ij} < \Delta d$), whereas it has no influence under 'normal' flow conditions.

For the two-dimensional problem described in this paper, the components of the artificial stress tensor $R_i^{\alpha\beta}$ for particle i in the reference coordinate system (x, y) are computed from the principal components R'^{xx}_i and R'^{yy}_i by the standard transformation:

$$R_i^{xx} = R'^{xx}_i \cos^2\theta_i + R'^{yy}_i \sin^2\theta_i \tag{65}$$

$$R_i^{yy} = R'^{xx}_i \sin^2\theta_i + R'^{xx}_i \cos^2\theta_i \tag{66}$$

$$R_i^{xy} = (R'^{xx}_i - R'^{yy}_i) \sin\theta_i \cos\theta_i \tag{67}$$

where the angle θ_i is defined by

$$\tan 2\theta_i = \frac{2\sigma_i^{xy}}{\sigma_i^{xx} - \sigma_i^{yy}} \tag{68}$$

DOI: 10.1002/nag

where σ_i^{xx}, σ_i^{yy} and σ_i^{xy} are components of stress tensor of particle i in the reference frame. The diagonal components of the artificial stress tensor in principle axes x', y' are, according to Gray *et al.* [23], calculated by

$$R_i'^{xx} = \begin{cases} -\varepsilon \dfrac{\sigma_i'^{xx}}{\rho_i^2} & \text{if } \sigma_i'^{xx} > 0 \\ 0 & \text{otherwise} \end{cases} \tag{69}$$

where ε is a small constant parameter ranging from 0 to 1 and $\sigma_i'^{xx}$ is diagonal stress tensor of particle i along the principal axis x'. The constant parameter ε in this paper will be chosen based on tests, although Gray *et al.* [23] suggested that $\varepsilon = 0.3$ is the best value for elastic solid. The same rule is applied to evaluate $R_i'^{yy}$ by simply replacing xx with yy. The diagonal components $\sigma_i'^{xx}$ and $\sigma_i'^{yy}$ of stress tensor of particle i in the principle coordinate can be calculated in terms of those in the reference frame by the following relations:

$$\sigma_i'^{xx} = \cos^2\theta_i \sigma_i^{xx} + 2\cos\theta \sin\theta \sigma_i^{xy} + \sin^2\theta \sigma_i^{yy} \tag{70}$$

$$\sigma_i'^{yy} = \sin^2\theta_i \sigma_i^{xx} - 2\cos\theta \sin\theta \sigma_i^{xy} + \cos^2\theta \sigma_i^{yy} \tag{71}$$

The same rules are applied to evaluate the artificial stress tensor for particle j by simply replacing subscript i by subscript j. The above artificial stress term, according to Monaghan [22] and Gray *et al.* [23], introduced negligible errors into the calculation results. This term only activates in the tensile stress region where particles clump unphysically.

4.4. Boundary conditions

SPH simulation may encounter the problem of *particle deficiency* near or on the boundary. For particle near or on the boundary, only neighboring particles inside the boundary contribute to the SPH summation for the gradient calculations, and no contribution comes from the outside since there are no particles beyond the boundary. This one-sided contribution leads to inaccurate solutions. In order to resolve this problem, a number of attempts have been proposed using different techniques. However, the most common approach in current SPH literature is still based on virtual (or ghost) particles [7, 8, 37]. In this paper, we deal with two types of boundary conditions: a solid boundary condition and a symmetric boundary condition.

To simulate the solid boundary, three layers of virtual particles, called 'boundary particles', are generated in the boundary region parallel to the solid wall, with the first layer $\Delta d/2$ outside the boundary as illustrated in Figure 3. These boundary particles have the same spatial separation Δd as real particles and their density is set equal to the reference density, ρ_0, of real particles. As in the work of Morris *et al.* [8], boundary particles contribute to the usual SPH expression for velocity and stress gradients. However, unlike Morris *et al.* [8], it is not necessary to evolve the density of boundary particles in the current application. The no-slip boundary condition is guaranteed by employing the method proposed by Morris *et al.* [8], which can be dated back to the original work by Takeda *et al.* [7]. For each fluid particle A, the normal distance d_A to the boundary is calculated. This normal distance is used to define a tangent plane from which the normal distance d_B to each boundary particle B is calculated. Then an artificial velocity $v_B = -(d_B/d_A)v_A$ is applied to the boundary particle B by the assumption of zero velocity condition on the plane itself. This artificial velocity v_B is then used for the evaluation of the velocity gradients of real particles near or on the

DOI: 10.1002/nag

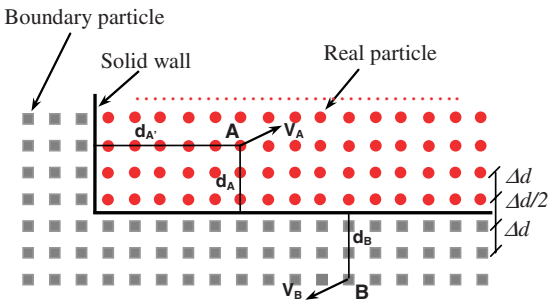

Figure 3. Initial particles arrangement and treatment of solid boundaries.

solid boundary, although not to locate the boundary particles, which move with the solid boundary. The relative velocity between real and boundary particles is

$$v_{AB} = v_A - v_B = \beta(v_A - v_{wall}) \tag{72}$$

and the artificial velocity of boundary particles on the moving boundary can be assigned via

$$v_B = (1-\beta)v_A + \beta v_{wall} \tag{73}$$

where

$$\beta = \min\left(\beta_{max}, 1.0 + \frac{d_B}{d_A}\right) \tag{74}$$

in which β_{max} is used to exclude the extremely large value of artificial velocity when real particles get too close to the solid boundary. According to Morris *et al.* [8], $\beta_{max} = 1.5$ gives good results for simulating low Reynolds number planar shear flows. In this study, good results are obtained for $\beta_{max} = 1.5$–2.

The above treatment of solid wall is not sufficient for the current SPH applications to elastic–plastic flows; it is also necessary to assign some stress values to the boundary particles when evaluating the summation in Equation (63). There have been a number of ways to assign stress values to boundary particles, the most general being derived by Randles and Libersky [37]. Herein, we use a simpler approach that is able to capture stress fluctuation and gives smooth stress profile of particles near the solid boundary. Our approach is based on the assumption of locally uniform distribution of stress on the solid boundary, which leads to the following way to assign stress components to boundary particles. For a given real particle i, if boundary particle j is a neighbor of particle i, then the stress tensor of particle i will be assigned to that of particle j:

$$\sigma_j^{\alpha\beta} = \sigma_i^{\alpha\beta} \quad \text{if } j \text{ is a neighbor of particle } i \tag{75}$$

Therefore, when a real particle approaches the solid boundary, its support domain in the boundary region will be in a state of uniform stress having the same magnitude as the stress tensor of the considered real particle. This approach to assign the stress tensor for boundary particles is straightforward and can save much computational time compared with other methods since this work can be performed together with the above procedure to extrapolate the virtual velocity of

DOI: 10.1002/nag

boundary particles. Our simulation tests have demonstrated that this approach works well in the current application and gives smooth stress contours for particles near the solid boundary.

The symmetric boundary condition in this study is modeled by using ghost particles, following Libersky and Petschek [3]. In this paper, the term 'ghost particles' refers to artificial particles that enforce the symmetric boundary condition, whereas 'boundary particles' enforce the no-slip condition at solid boundaries. The ghost particles are constructed in the following way. For each real particle i that is located within the distance of kh_i from the boundary, a ghost particle is placed symmetrically on the outside of the boundary. These ghost particles will have the same physical properties as real particles except velocity and stress tensor. The velocity of ghost particles normal to the boundary (normal velocity) is taken as minus that of real particles in order to prevent the real particles from penetrating the boundary. On the other hand, the velocity of ghost particles tangent to the boundary (shear velocity) is set equal to that of real particles in order to simulate the free-slip boundary condition on the symmetry plane. The stress tensor of ghost particles is set according to the following relations:

$$\sigma_{\mathrm{G}}^{\alpha\beta} = \begin{cases} \sigma_R^{\alpha\beta} & \text{if } \alpha = b \\ -\sigma_R^{\alpha\beta} & \text{if } \alpha \neq b \end{cases} \tag{76}$$

Since the ghost particles satisfy free-slip condition on the symmetric plane, they can also be used to simulate a solid boundary with the free-slip condition. In such a circumstance, the stress tensor of ghost particle should be taken identical to that of real particle rather than using the expression in Equation (76). The ghost boundary particles work well for straight boundaries but introduce errors for curveted boundaries [8].

4.5. Evaluation of stress on a solid boundary

In SPH, the field variables at a point or at a specific position are normally obtained by adopting an interpolation process over neighboring particles; however, it is not straightforward to evaluate stresses acting on a solid boundary. We have tried several ways to extrapolate stress on the solid boundary and the following way, which is based on the corrective smooth particle method [34], gives us the best results. The average stress applied on the solid boundary can be estimated by the following equation:

$$P = \frac{\int_{n=1}^{M} P_n \, \mathrm{d}s_n}{\sum_{n=1}^{M} \mathrm{d}s_n} \tag{77}$$

where P is the average total stress applied on the solid boundary; M is the number of elements or particles on the solid boundary; ds is the area of surface elements that lie between each pair of particles on the solid boundary, and P_n is the local stress at the corresponding point n on the solid boundary. This local stress might be estimated by directly extrapolating stress from the interior real particles according to

$$P_n = \sum_{i=1}^{N} \frac{m_i}{\rho_i} P_i W_{ni} \tag{78}$$

where i runs over neighboring particles of n located within the distance of kh from particle n, W is the smoothing function taken here to have the same form as the cubic spline function although

DOI: 10.1002/nag

other forms, such as Gaussian function, can be used. However, estimation of local stress from Equation (78) does not give a correct solution since there are no contributions of stress from outside the solid boundary. Therefore, the corrective smoothed particle method [34] is applied here. Accordingly, Equation (78) is replaced by

$$P_n = \frac{\sum_{i=1}^{N} \frac{m_i}{\rho_i} P_i W_{ni}}{\sum_{i=1}^{N} \frac{m_i}{\rho_i} W_{ni}} \tag{79}$$

The term appearing in the denominator actually comes from a Taylor expansion of P around n and provides the desired correction near the solid boundary. For further details on the corrective SPM, see [19, 34].

4.6. Time integration

In order to solve the above set of discrete SPH equations in the form of ordinary differential equations, standard techniques such as the second-order accurate LF, predictor–corrector and Runge–Kutta (RK) schemes, etc. can be used to integrate the field variables at every particle. In practice, the LF algorithm is very popular for its low memory requirement and the efficiency for one force per step; hence, it is adopted in this paper [19]. In this method, the field variables, which include velocities (v), density (ρ), stress tensor ($\sigma^{\alpha\beta}$) and positions of particle are updated by using the following equations:

$$\rho_{n+1/2} = \rho_{n-1/2} + \Delta t \left(\frac{\mathrm{D}\rho}{\mathrm{D}t}\right)_n \tag{80}$$

$$v_{n+1/2} = v_{n-1/2} + \Delta t \left(\frac{\mathrm{D}v}{\mathrm{D}t}\right)_n \tag{81}$$

$$\sigma^{\alpha\beta}_{n+1/2} = \sigma^{\alpha\beta}_{n-1/2} + \Delta t \left(\frac{\mathrm{D}\sigma^{\alpha\beta}}{\mathrm{D}t}\right)_n \tag{82}$$

$$x_{n+1} = x_n + \Delta t\, v_{n+1/2} \tag{83}$$

In order to keep the calculations consistent at each subsequent time step, at the start of each time step, the density, the velocity and the stress tensor of each particle need to be predicted at half a time step to coincide the position t_n. After each calculation step, the stress tensor of material must be checked for violations of the yield criterion, i.e. the stress state of material exceeds the apex or the yield surface. If so, the return mapping algorithm described in Section 3.3 will be applied to recover consistency with the soil constitutive model.

The stability of the above LF integration scheme is governed by the so-called Courant–Friedrichs–Levy condition, which allows a time step proportional to the smoothing length. In this work, the following condition is used to determine the size of time step:

$$\Delta t \leqslant C_{\mathrm{cour}} \left(\frac{h}{c}\right) \tag{84}$$

DOI: 10.1002/nag

where c is the sound speed of the media. In the standard SPH method, the sound speed c is often chosen to yield density fluctuations of about 1% [6]. This choice of sound speed is considerably slower than the physical velocity and, therefore, can save computational time. In this study, the maximum physical sound speed in soil ($c=600\,\mathrm{m/s}$) is applied in the computations. This will result in a very small time step compared with the standard SPH method. The very small time step associated with the updated Lagrangian formulation of the dynamical equations will reduce the inaccuracy caused by the lack of incremental objectivity that results from the use of small deformation theory in this paper. The Courant coefficient is chosen to be $C_{\mathrm{cour}}=0.2$.

5. RESULTS AND DISCUSSIONS

In this section, SPH will be applied to simulate geotechnical problems. Two main problems will be considered to test the abilities of the proposed method. First, SPH will be applied to simulate the gravitational flow following soil collapse, which involves an extremely large deformation and failure of soil. Through this study case, we will show that SPH encounters the tensile instability problem at large deformation, especially for cohesive soil. Discussions on how this numerical instability can be removed will be given and proved through numerical tests compared with experimental data. Next, SPH is applied to simulate the standard bearing capacity problems, which are commonly found in geotechnical engineering. The validity of this application will be checked by comparing our SPH numerical results with the FEM solutions conducted by Chen and Mizuno [24].

5.1. Large deformation and post-failure of non-cohesive soil by SPH simulation

In this simulation, a total of 5000 real particles are used to form an initial rectangular soil area 4 m in length and 2 m in height with an initial smoothing length of 0.048 m, and 1800 boundary particles are used to generate the solid boundaries. These soil particles have a density of $1850\,\mathrm{kg/m^3}$, elastic bulk modulus of 1.5MPa, and friction angles of 25, 45 and 65°, respectively, for three computational cases. The non-associated plastic flow rule soil model is adopted in these simulations to describe the behavior of granular material. Simulations are carried out with artificial viscosity terms α_Π and β_Π, both taken as 0.1. The return mapping algorithm, which includes the tension cracking treatment and stress-rescaling procedure, is also applied in these simulations.

Figure 4 shows the failure process of non-cohesive soil through SPH simulation with different friction angles at representative times. From this figure, it can be seen that soil collapses naturally in the same way as granular material. No tensile instability was found in these SPH applications for elastic–plastic flows even though a high friction angle was applied. As could be seen, large deformation and failure of soil can be simulated well through the SPH framework. After collapse, soil particles move to the right, experience large deformations and finally form an angle of repose. The failure patterns of soil particles are visualized clearly through the deformation of initially square grids of 'tracers' plotted on the soil areas. The reposed angle obtained in each simulation is not precisely equal to friction angle, but increases with it. We will show in the following section that the reposed angle of granular material obtained from experiment is also different from the friction angle obtained from one-dimensional shear box test. In addition to the above solutions, we also did the simulations without using tension cracking treatment. Results are still stable for small friction angle soil but become unstable when using high friction angle. Soil in latter simulations acts more like cohesive soil than the usual granular material. This indicates that the original SPH

DOI: 10.1002/nag

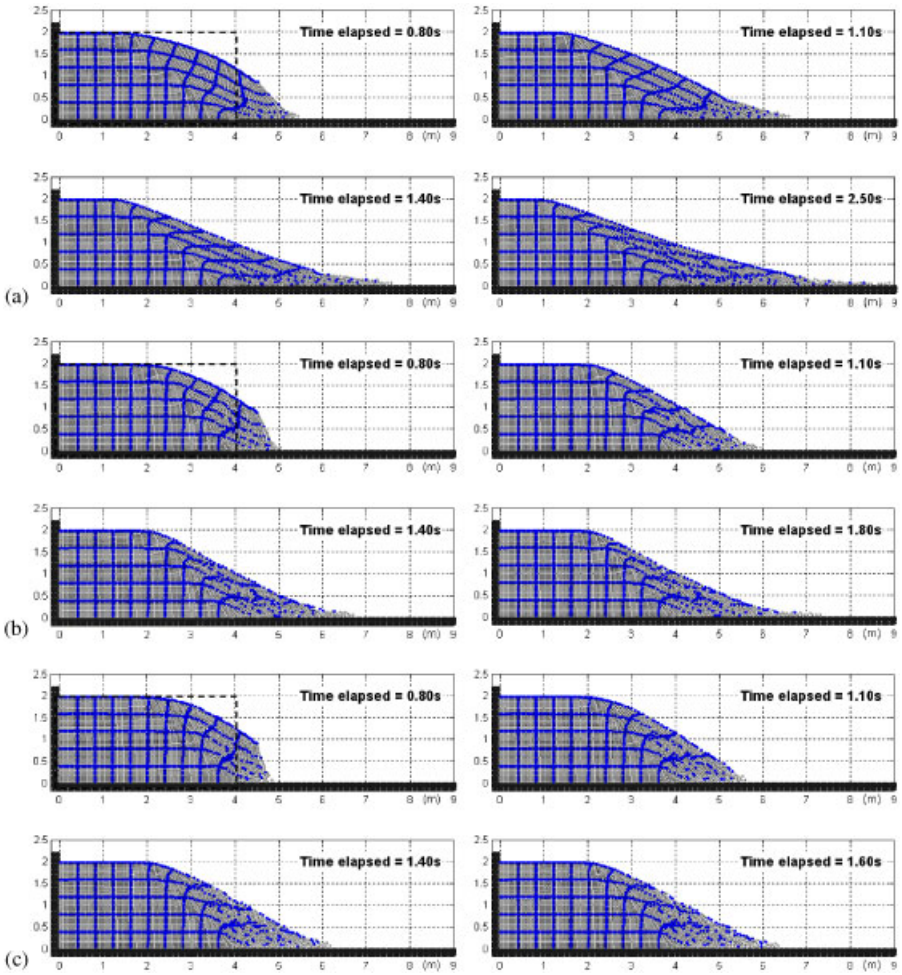

Figure 4. Failure process of non-cohesive soil by SPH simulation at representative times: friction angle of (a) $\phi = 25°$; (b) $\phi = 45°$; and (c) $\phi = 65°$.

method needs additional improvements to apply to soils. The validity of this tension cracking treatment in the SPH simulations will be further discussed in the following section together with experimental data.

5.2. Comparing SPH simulation and two-dimensional experiment of soil collapse

To validate the above numerical solutions, a simple experiment of soil collapse was conducted and compared with the SPH solution. Since the SPH simulation is carried out under two-dimensional condition, experiments should also be conducted under such conditions. For this purpose, we decided to use small aluminum bars of diameters 1 and 1.5 mm, length 50 mm and density 2650 kg/m^3, to model the soil. This soil model was initially arranged into a rectangular area

DOI: 10.1002/nag

(200×100 mm), which is generated by standing two flat solid rods (walls) on a flat surface. The above soil scale was decided after a number of trial tests, bigger scale will lead to unstable movement of soil particles during the failure process, i.e. aluminum bars will not move horizontally. A reference grid was set behind the soil volume, out of contact with the soil particles, to measure surface configuration of soil particles after collapse. To visualize the failure pattern of soil particles, square grids (20×20 mm) were plotted on the specimen. The experiment was started by quickly removing the right wall horizontally to the right.

The parameters for the soil constitutive model include cohesion coefficient (c), friction angle (ϕ) and elastic bulk modulus (K). To determine realistic values, a shear box test on aluminum bars also conducted. Four experiments were carried out at the low loading conditions of 32.7, 65.4, 98.1 and 130.8 kPa. The resulting stress–strain relationships, shown in Figure 5, allow us to specify the peak shear stress at each loading condition. The yield surface was then generated by connecting these peak shear stresses, thereby giving us the values of cohesion coefficient and friction angle.

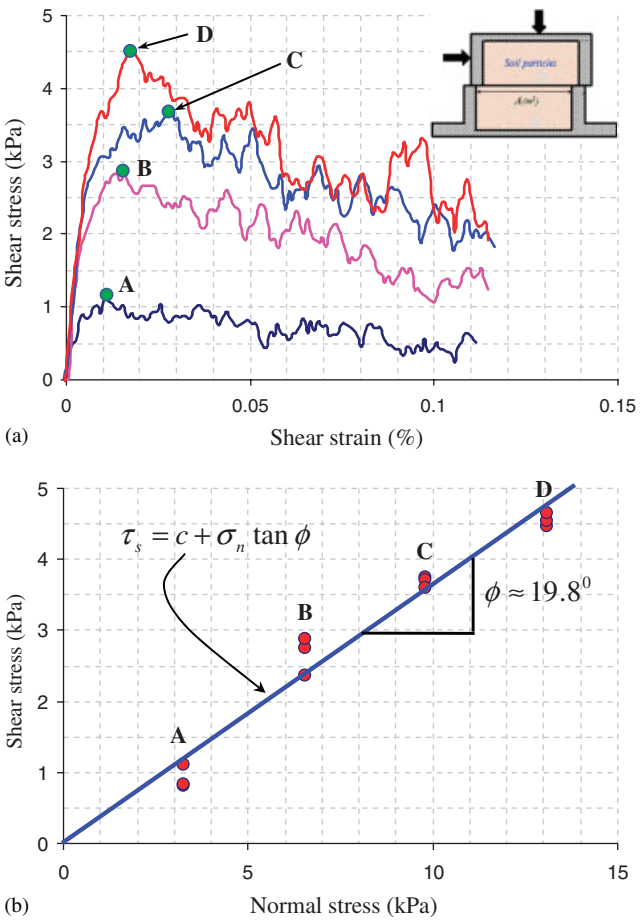

Figure 5. Typical stress–strain relationships (a) and yield surface (b) of soil model obtained from the shear box test.

DOI: 10.1002/nag

It can be seen that the yield surface passes through the origin, which confirms the non-cohesive property of aluminum bars. The friction angle was found to be about $\phi = 19.8°$. The elastic properties can be also obtained from the stress–strain relationships. These lines allow us to specify an average value of shear modulus G, which corresponds to the slope of elastic part, and with an assumption of constant Poisson's ratio $v = 0.3$, the average bulk modulus can be determined as $K \approx 0.7\,\text{MPa}$.

The friction angle and bulk modulus of aluminum bars obtained from the above experiment were then employed in the SPH simulation using 3200 particles arranged in the same configuration as the experiment sample. The non-associated flow rule soil model was adopted in this simulation to describe the behavior of granular material. The artificial viscosity was specified the same as the previous simulations, and the no-slip boundary condition was employed to model the solid boundaries. The comparison between experiment and simulation is given in Figure 6, which exhibits excellent agreement between SPH simulation and experimental result. The deformation pattern of soil in simulation looks almost identical to that of experiment. As indicated in Figure 6(d), good agreement between simulation and experiment is found not only for the surface configurations but also for the failure lines that separate the deformed and non-deformed areas. In addition, the reposed angle of soil collapse in experiment is also less than the internal friction angle of 19.8° obtained from the shear box test. This result also agrees with those obtained from the earlier SPH simulations. The good agreements between simulation and experiment indicates that the current SPH model works well for non-cohesive soil and confirms that the above elastic–plastic soil model works well in the SPH framework for large deformation and post-failure problems.

The tension cracking treatment is now validated by again simulating the above experimental problem without this treatment. Result obtained from this simulation, as shown in Figure 7(a), is compared with the usual simulation where the tension cracking treatment is taken into account. The dashed line in these images is the final surface configuration of soil particles in experiment. As can be seen, when the tension cracking treatment is switched on, simulation result for surface configuration is in good agreement to that of experiment. On the other hand, differences in surface configuration and displacement of soil particles appear when the tension cracking treatment is switched off. The effect of the tension cracking treatment can be further observed by increasing the friction angle to 45°, which is similar to the friction angle of relatively dense Toyoura sand, while keeping constant other parameters and the initial soil configuration. The results of this simulation are shown in Figure 7(b). It can be observed clearly that soil behaves as a nature granular material when the tension cracking treatment is adopted; conversely, the result becomes unusual without this treatment. Soil in this case behaves more like cohesive soil than granular material. In addition to the above unusual behavior, slightly unrealistic fracture is also observed on the free surface of this material during collapse. This indicates that SPH tensile instability occurred in this simulation and it becomes more serious as the friction angle is increased (results were not shown in this paper). However, the fracture was completely removed by adopting the tension cracking treatment as shown by the left of Figure 7(b) as well as by the results in the previous simulation with high friction angle of 65°. It should be noted that the artificial stress method described in Section 4.3 will have no effect in non-cohesive soil since there is no tension stress state after employing the return mapping algorithm. Therefore, we can switch off this term in non-cohesive soil simulation. From the above validation, it can be concluded that the tension cracking treatment not only kept soil moving in accord with the soil constitutive model but also use to remove tensile instability problem in non-cohesive soil.

DOI: 10.1002/nag

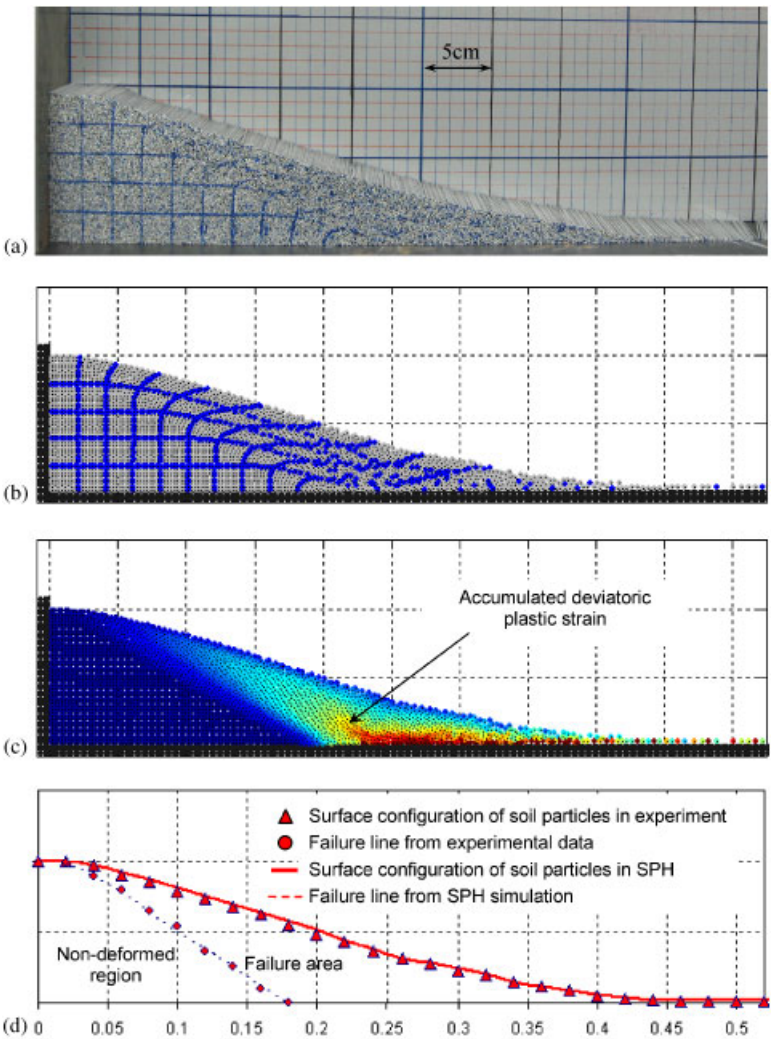

Figure 6. Comparison between experiment and SPH simulation of non-cohesive soil failure: (a) experimental result; (b) SPH simulation result; (c) accumulated deviatoric plastic strain from simulation; and (d) final surface configurations and failure lines in experiment and simulation.

5.3. Large deformation and failure of cohesive soil

In this section, we extend the above SPH model to test this method with cohesive soil. To do so, we again simulate the problems described in Section 5.1 using the same particles configuration and soil parameters except that the value of cohesion is now increased to 5 kPa. Here, we only consider the case with a friction angle of 25°; similar results were also obtained in simulations using different friction angles. The results of this application are shown in Figure 8 where different values of ε are considered.

DOI: 10.1002/nag

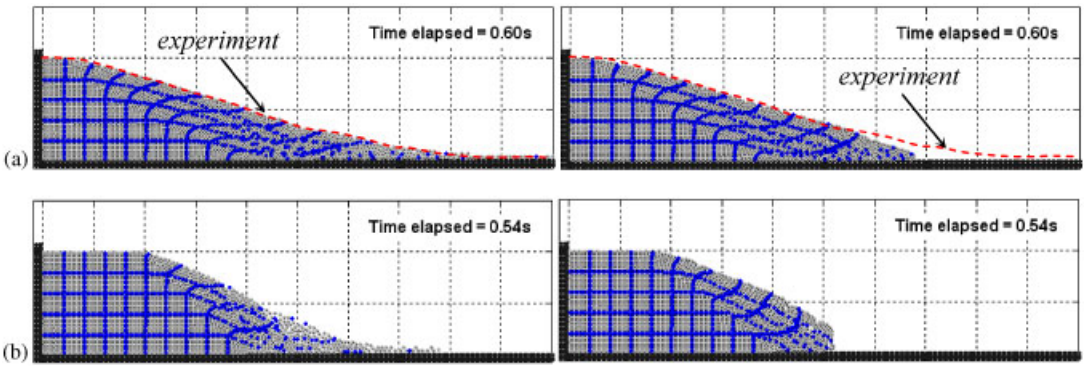

Figure 7. Effect of the tension cracking treatment on numerical solutions for non-cohesive soil with friction angle of (a) $\phi = 19.8°$ and (b) $\phi = 45°$. The left images are the SPH simulation using the tension cracking treatment, while right ones are results without employing this treatment. The dashed lines in (a) indicate the surface configuration of soil particles obtained from experiment.

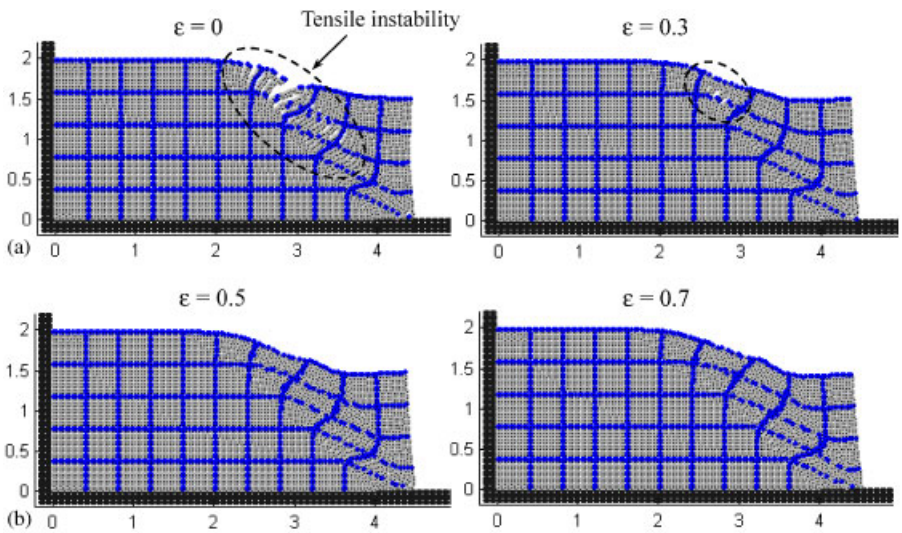

Figure 8. SPH tensile instability in cohesive soil was removed by using the artificial stress method. Different coefficients for the artificial stress term are investigated to find the best value. The exponent n was kept constant at 2.55, while the coefficient ε was increased from 0 to 0.7. The best result was found at $\varepsilon = 0.5$.

From this figure, it can be seen clearly that without using artificial stress term ($\varepsilon = 0$), SPH could not handle the large deformation and failure of cohesive soil without unrealistic fracture at the soil surface, the so-called tensile instability. Herein, the method that was successfully applied to remove the tensile instability in non-cohesive soil, i.e. the tension cracking treatment, could not resolve this problem in cohesive soil. This can be explained due to the existence of tensile stress states ($I_1 > 0$) in cohesive soil, i.e. on the left side of $\sqrt{J_2}$-axis in $(-I_1, \sqrt{J_2})$ plane, even if the tension cracking treatment was already employed. Our numerical tests have shown that the more

DOI: 10.1002/nag

serious fracture will be observed in the simulation without using this tension cracking treatment. By adding artificial stress term, which was described in Section 4.3, into the momentum equation, the tensile instability is reduced by taking $\varepsilon=0.3$ and is completely removed with $\varepsilon=0.5$ and 0.7. The exponent n was kept constant at $n=2.55$ in these simulations. For elastic solid, it has been shown through the results of Gray *et al.* [23] that taking $n=4$ is optimal, in which case $\varepsilon=0.3$ is large enough. However, for elastic–plastic soil, we found that this choice is not suitable; using $n=4$ with smoothing length h=1.2Δd results in numerical instability due to a strongly repulsive force between particles, which are in tension. For example, the above choice will make the repulsive force increase by a factor of about $\sim$42 as r_{ij} decreases from Δd to zero. Our recommendation to remove this tensile instability in the current SPH application for cohesive soil is $n=2.55$ and $\varepsilon=0.5$ for $h=1.2\Delta d$. This selection of parameters has been decided after carefully investigating a number of tests on this problem with both smaller- and larger-scale simulations. From the above simulation results, it may be concluded that the tensile instability is more significant in cohesive than in non-cohesive soil.

After removing the tensile instability problem, the simulated soil particles fail naturally as shown in Figure 9. The development of a shear band is observed clearly through the deviatoric plastic strain. The results show that most soil particles that experienced large shear deformation are associated with high plastic strain, while this is not observed in the non-shearing particles. The plastic area expands during the failure process until the soil particles stop moving at around 2 s after collapse. Moreover, if we focus attention on the position of 'fracture' shown in Figure 8, it can be seen that the tensile instability occurred in the plastic region of soil.

We repeated these simulations for cohesive soil without using the artificial stress method. Instead, we increased the values of artificial viscosity to $\alpha_\Pi=1$ and $\beta_\Pi=1$; this suppresses the unrealistic fracture obtained in the previous simulation without completely removing it. By increasing α_Π and β_Π further, this tensile instability may be removed; however, this is not a good way to remove the tensile instability problem since a large artificial viscosity will affect the flow and thus soil will deform differently. The artificial viscosity described in this paper should be only used to stabilize the numerical scheme.

By increasing the value of cohesion, the soil particles in SPH simulation will stand without deforming; therefore, the tensile instability will not occur. This result is also natural in soil mechanics. Similar results are also obtained for large-scale simulation.

5.4. Simulation of bearing capacity problems and comparing to Chen and Mizuno [*24*]

In this section, the accuracy of the above SPH application for geo-material is examined by comparing with a grid-based method, i.e. the FEM. Specifically, the standard problem of bearing capacity is conducted and compared with the analytical and FEM solutions by Chen and Mizuno [24]. The following is the configuration considered by Chen and Mizuno [24]: a 3.14 m (10.28 ft) wide strip footing bears on a shallow stratum supported by a rigid, perfectly rough base. The horizontal stratum extends 7.32 m (24 ft) horizontally from the footing center, and the depth of the stratum is 3.66 m (12 ft). The vertical boundary was assumed to be perfectly smooth and rigid, and the strip footing was assumed to be rigid and perfectly rough. The soil constants used in the FEM calculation are Young's modulus $E=207$ MPa (3000 psi), Poisson's ratio $v=0.3$, cohesion $c=69$ kPa (10 psi), angle of internal friction $\phi=20°$. The soil weight is neglected. FEM analyses were carried out by means of Drucker–Prager model with the associated and non-associated flow rules under plane strain conditions.

DOI: 10.1002/nag

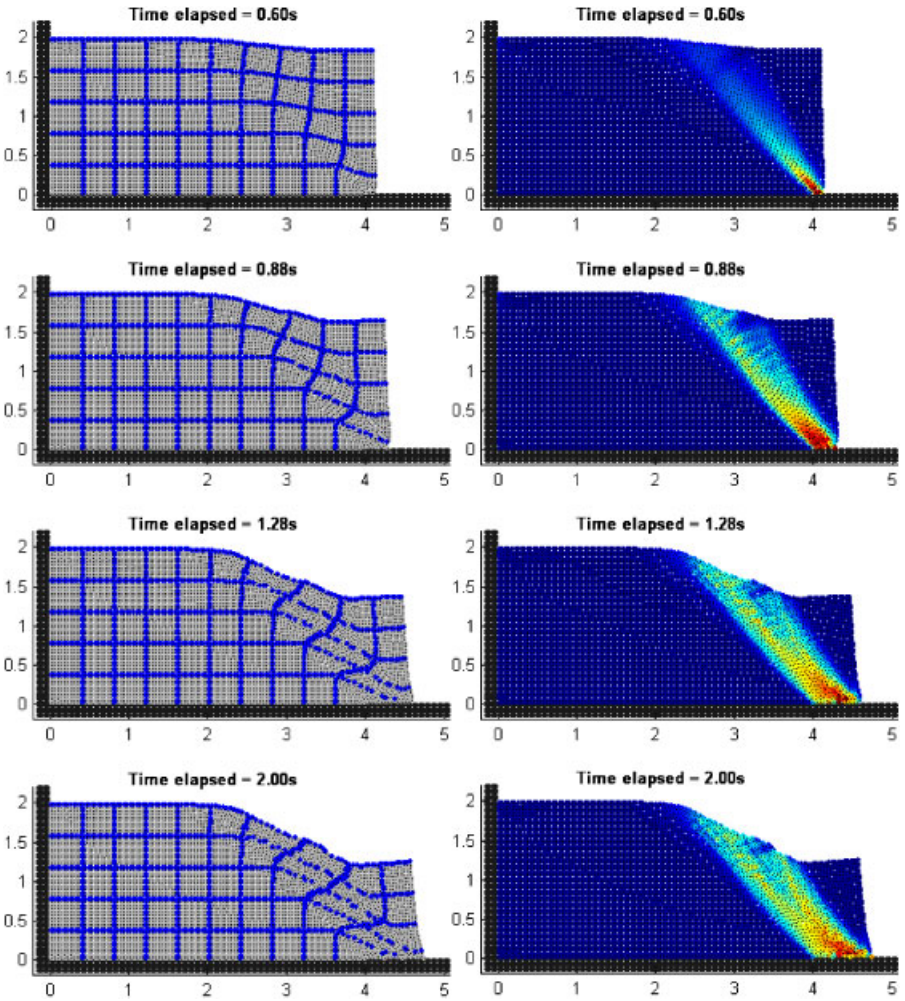

Figure 9. Deformation pattern of cohesive soil (left images) and the corresponding accumulated deviatoric plastic strain (right images) at representative times after removing the SPH tensile instability problem.

To conduct the above bearing capacity model by SPH, the symmetric boundary condition is adopted at the center of the stratum, and only half of the stratum is taken into consideration. A total of 7371 SPH particles are arranged in a rectangular lattice to generate the half stratum with an initial smoothing length of 0.0732 m. These particles have the same material properties as the soil model used in the FEM simulation. 'Boundary particles' with no-slip boundary condition are used to model the rigid, rough base and strip footing. On the other hand, the 'ghost particles' that satisfy the free-slip boundary condition are assigned to the vertical boundary. Artificial viscosity is used in these simulations, with $\alpha_\Pi = 1$ and $\beta_\Pi = 1$. A smaller value of α_Π results in stress fluctuation since large cohesive coefficient is considered. The return mapping algorithm and artificial stress method are also employed to remove the numerical instability at large deformation loading.

DOI: 10.1002/nag

To match the neglect of soil weight in FEM, the gravitational force is set to zero; therefore, there is no need to solve the continuity equation. Even so, it is still necessary to set a reference density for soil particles in order to remove the numerical divergence from the SPH momentum equation, and this density was taken at $1850\,kg/m^3$ in these applications. Tests gave almost identical results for reference densities between 1000 and $2750\,kg/m^3$. The loading speed of the strip footing should be taken small enough to ensure the accurate solutions and is taken to be 2 cm/s for the problem described in this paper. The average pressure applied beneath the footing is evaluated by using the method described in Section 4.5.

Figure 10 compares the load–displacement relationships of SPH and FEM simulations for both associated and non-associated flow rules along with the limit analysis (slip line), Prandtl and Terzaghi solutions. In both FEM and SPH simulations, the non-associated Drucker–Prager model gives a softer response of limit load than the corresponding associated model. These curves rise linearly to about 449 kPa in both methods and then show nonlinear behavior, which corresponds to plastic loading, until they reach the collapse loads. During plastic loading, the load–displacement curves obtained from the SPH simulations are slightly lower than those of the corresponding FEM simulations, although the limit load obtained from the non-associated soil model in SPH almost matches that of FEM. This slight difference may result from the treatments of boundary condition on the strip footing, where the shear stress of particles right beneath the footing in FEM simulation was constrained to zero, while this was not done in SPH. In addition, soil particles in contact with the footing in FEM simulation were prevented from horizontal movement; on the other hand, particles near the footing edge in SPH are still able to move in this direction, although not freely due to the no-slip boundary condition. Another cause may be the neglect of soil weight employed in SPH simulation since SPH is more suitable for dynamic problems than static ones. Overall, however, the results obtained from the SPH simulations agree well with those obtained by FEM simulations for the same soil models and differ quantitatively from those obtained with

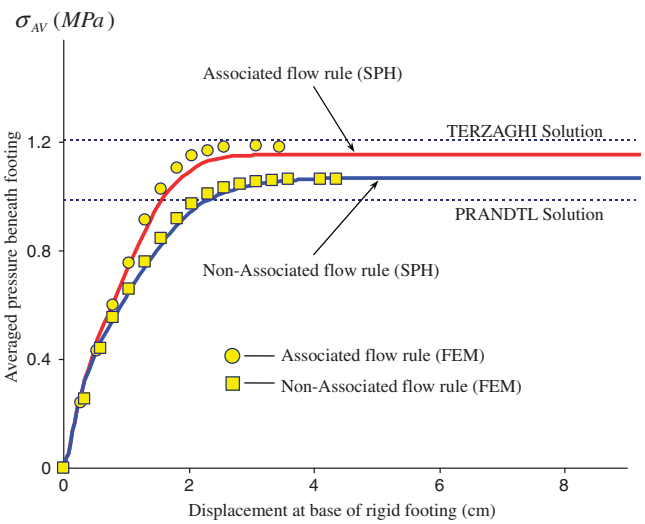

Figure 10. Load–displacement curves by Drucker–Prager models with associated and non-associated flow rules in SPH and FEM [24] simulations.

DOI: 10.1002/nag

the FEM by a maximum of 2%. Furthermore, if we compare SPH with the analytical results, it can be seen that both models predict limit loads that lie between the Prandtl and Terzaghi solutions.

Our numerical tests showed that the configuration chosen by Chen and Mizuno [24] was not sufficiently wide to avoid boundary effects. Therefore, we continue to test our method in this application by extending the horizontal extent of the stratum to 10.065 m (33 ft). The velocity field and the corresponding accumulated deviatoric plastic strain of soil particles at 30 cm footing displacement are presented in Figure 11. It can be seen that the magnitude of the velocity field in the associated model is much larger than that predicted by the non-associated model. This is due to the large amount of dilatancy allowed by the associated model which, in contrast to the non-associated model, has zero dilatancy angle in the current simulations. The Prandtl failure mechanism was also obtained in both models. These SPH results agree well with those obtained by Chen and Mizuno [24]. In addition, the contour of accumulated deviatoric plastic strain at 30 cm displacement of the footing show clear strain localization in the case of associated soil model, whereas this strain localization has not yet formed clearly in the case of the non-associated model. The results obtained here show that the strain localization can be displayed clearly through SPH simulation even at the large deformation, unlike FEM. Simulation can be continued as long as desired without encountering any problems.

From the above benchmark results, it could be said that the current SPH model can be readily extended to general geotechnical problems under plane strain conditions. SPH can give similar results to FEM simulation, while additionally possessing the capability to handle large deformation without any difficulties.

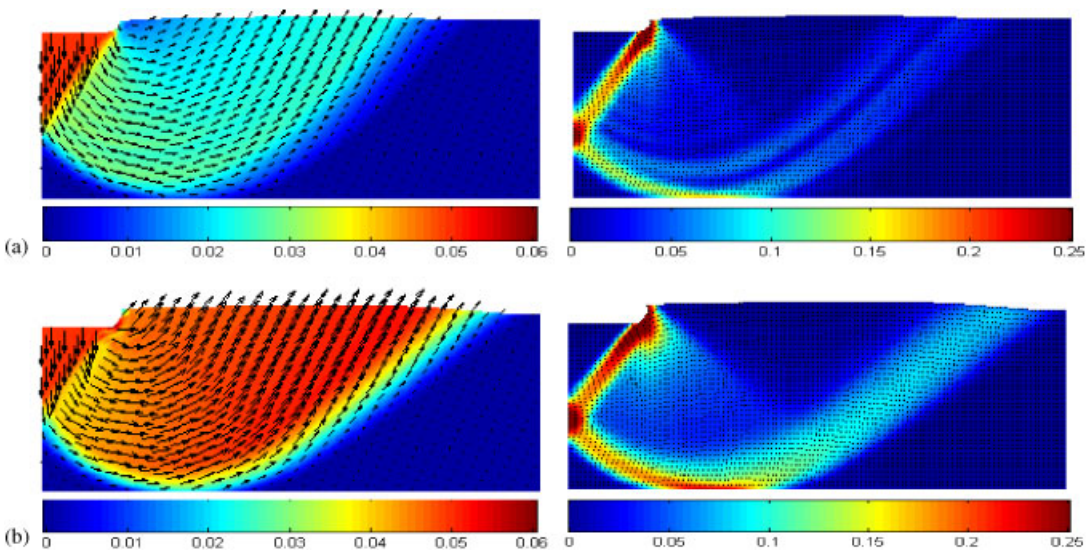

Figure 11. Results of bearing capacity in SPH simulation after extending the horizontal extent of the stratum to 10.065 m: velocity field (left images) and corresponding accumulated contours of deviatoric plastic strain (right images) at 30 cm displacement of the footing. (a) Non-associated flow rule model and (b) associated flow rule model.

DOI: 10.1002/nag

6. CONCLUSIONS

The development of SPH to resolve the large deformation and post-failure of geomaterial has been described. The Drucker–Prager model, with associated and non-associated plastic flow rules, has been implemented for the first time into the SPH framework. Applications of SPH to simulate the large deformation and post-failure flows of non-cohesive and cohesive soils have been presented and discussed. From this study, we concluded that the original SPH method, which has been successfully applied to a vast range of problems, could not be directly applied to simulate elastic–plastic soil behavior because of the SPH tensile instability problem, which resulted in unrealistic fracture at the soil surface at large deformation. In non-cohesive soil, this problem was almost unrecognizable at small friction angle material; however, mild tensile instability developed when a relatively high friction angle was applied. This paper showed that using the treatment of tension cracking, this problem can be completely removed so as to obtain realistic behavior of granular material through SPH simulation.

For cohesive soil, the SPH method encountered a serious tensile instability problem that leads to the failure of the computation. The tension cracking treatment, which removed the tensile instability in non-cohesive soil, could not resolve this problem. By using the artificial stress method [22, 23], this tensile instability could be overcome; however, the present application requires values for the coefficients for the artificial stress term that differ significantly from those habitually used in SPH of elastic dynamics.

Finally, the numerical results obtained from this paper showed good agreements with both experiment and FEM solution [24]. Furthermore, the development of shear bands during failure, which is generally difficult to simulate by FEM, can be also predicted clearly by the SPH method. The biggest advantage of SPH is that it can handle large deformation and failure without any difficulties. These results suggest that SPH could be a potential method for solving large deformation and post-failure of geomaterial. In order to further enhance the SPH application for geomechanics, it is necessary to continue extending this method to more general soil constitutive models such as elasto-plastic models with hardening/softening, elasto-viscous plastic model, Cap models, etc. These can be reliably handled by the SPH framework presented in this paper. In addition, to improve the accuracy of the SPH method for the simulation of large deformation and post-failure of geomaterial, which suffered from the use of small deformation theory in this paper, the finite deformation formulations should be implemented into the SPH framework in order to keep the objectivity of strain and stress measures. In this study, the inaccuracy caused by the lack of incremental objectivity is not significant as a very small time step was taken and the updated Lagrangian formulations were used.

APPENDIX A

The general stress–strain relationship of an elastic–perfectly plastic Drucker–Prager soil model can be derived in the following way. The total strain rate tensor in Equation (12) has the following form:

$$\dot{\varepsilon}^{\alpha\beta} = \frac{\dot{s}^{\alpha\beta}}{2G} + \frac{1-2v}{3E}\dot{\sigma}^{\gamma\gamma}\delta^{\alpha\beta} + \dot{\lambda}\frac{\partial g}{\partial \sigma^{\alpha\beta}} \tag{A1}$$

DOI: 10.1002/nag

This equation can be rewritten by replacing $\dot{I}_1 = \dot{\sigma}^{\gamma\gamma}$, leading to

$$\dot{\varepsilon}^{\alpha\beta} = \frac{\dot{s}^{\alpha\beta}}{2G} + \frac{\dot{I}_1}{9K}\delta^{\alpha\beta} + \dot{\lambda}\frac{\partial g}{\partial \sigma^{\alpha\beta}} \tag{A2}$$

Substituting $\dot{s}^{\alpha\beta} = \dot{\sigma}^{\alpha\beta} - \frac{1}{3}\dot{I}_1\delta^{\alpha\beta}$ into Equation (A2) and solving for $\dot{\sigma}^{\alpha\beta}$, the following stress–strain relationship can be obtained:

$$\dot{\sigma}^{\alpha\beta} = 2G\dot{\varepsilon}^{\alpha\beta} - 2G\dot{\lambda} + \frac{3K - 2G}{9}\dot{I}_1\delta^{\alpha\beta} \tag{A3}$$

The value of $\dot{I}_1$ can be derived by setting $\alpha = \beta$ in Equation (A2) leading to

$$\dot{I}_1 = 3K\left(\dot{\varepsilon}^{\gamma\gamma} - \dot{\lambda}\frac{\partial g}{\partial \sigma^{\alpha\beta}}\delta^{\alpha\beta}\right) \tag{A4}$$

Substituting Equation (A4) into Equation (A3), the general stress–strain relationship for an elastic–perfectly plastic material, Equation (13), can be derived as follows:

$$\dot{\sigma}^{\alpha\beta} = 2G\dot{e}^{\alpha\beta} + K\dot{\varepsilon}^{\gamma\gamma}\delta^{\alpha\beta} - \dot{\lambda}\left[\left(K - \frac{2G}{3}\right)\frac{\partial g}{\partial \sigma^{mn}}\delta^{mn}\delta^{\alpha\beta} + 2G\frac{\partial g}{\partial \sigma^{\alpha\beta}}\right] \tag{A5}$$

For the Drucker–Prager material, the yield and plastic potential functions are generally given by the following equations:

$$f(\sigma^{\alpha\beta}) = F(I_1, \sqrt{J_2}) - K = 0 \tag{A6}$$

$$g(\sigma^{\alpha\beta}) = G(I_1, \sqrt{J_2}) - K = 0 \tag{A7}$$

Hence, the derivative of these functions with respect to the stress tensor can be derived by

$$\frac{\partial f}{\partial \sigma^{\alpha\beta}} = \frac{\partial f}{\partial I_1}\frac{\partial I_1}{\partial \sigma^{\alpha\beta}} + \frac{\partial f}{\partial \sqrt{J_2}}\frac{\partial \sqrt{J_2}}{\partial \sigma^{\alpha\beta}} = \frac{\partial f}{\partial I_1}\delta^{\alpha\beta} + \frac{1}{2\sqrt{J_2}}\frac{\partial f}{\partial \sqrt{J_2}}s^{\alpha\beta} \tag{A8}$$

$$\frac{\partial g}{\partial \sigma^{\alpha\beta}} = \frac{\partial g}{\partial I_1}\frac{\partial I_1}{\partial \sigma^{\alpha\beta}} + \frac{\partial g}{\partial \sqrt{J_2}}\frac{\partial \sqrt{J_2}}{\partial \sigma^{\alpha\beta}} = \frac{\partial g}{\partial I_1}\delta^{\alpha\beta} + \frac{1}{2\sqrt{J_2}}\frac{\partial g}{\partial \sqrt{J_2}}s^{\alpha\beta} \tag{A9}$$

Substituting Equation (A9) into Equation (A5), the general stress–strain relationship for the Drucker–Prager material can be obtained as

$$\dot{\sigma}^{\alpha\beta} = 2G\dot{e}^{\alpha\beta} + K\dot{\varepsilon}^{\gamma\gamma}\delta^{\alpha\beta} - \dot{\lambda}\left[3K\frac{\partial g}{\partial I_1}\delta^{\alpha\beta} + \frac{G}{\sqrt{J_2}}\frac{\partial g}{\partial \sqrt{J_2}}s^{\alpha\beta}\right] \tag{A10}$$

where the plastic multiplier can be also derived by substituting Equations (A8)–(A9) into Equation (14) leading to

$$\dot{\lambda} = \frac{3K\dot{\varepsilon}^{\gamma\gamma}\dfrac{\partial f}{\partial I_1} + \dfrac{G}{\sqrt{J_2}}\dfrac{\partial f}{\partial \sqrt{J_2}}s^{mn}\dot{\varepsilon}^{mn}}{9K\dfrac{\partial f}{\partial I_1}\dfrac{\partial g}{\partial I_1} + G\dfrac{\partial f}{\partial \sqrt{J_2}}\dfrac{\partial g}{\partial \sqrt{J_2}}} \tag{A11}$$

DOI: 10.1002/nag

Equations (A10) and (A11) were derived using the following identities:

$$\delta^{\alpha\beta}\delta^{\alpha\beta}=3, \quad \dot{\varepsilon}^{\alpha\beta}\delta^{\alpha\beta}=\dot{\varepsilon}^{\gamma\gamma}, \quad s^{\alpha\beta}\delta^{\alpha\beta}=0 \tag{A12}$$

Finally, substituting Equations (16), (19) and (20) into Equations (A10) and (A11), the final stress relationship described in Equations (22)–(24) can be obtained.

REFERENCES

1. Lucy L. A numerical approach to testing the fission hypothesis. *Astronomical Journal* 1977; **82**:1013–1024.
2. Gingold RA, Monaghan JJ. Smoothed particle hydrodynamics: theory and application to nonspherical stars. *Monthly Notices of the Royal Astronomical Society* 1977; **181**:375–389.
3. Libersky LD, Petschek AG. Smoothed particle hydrodynamics with strength of materials. In *Proceedings of the Next Free Lagrange Conference*, vol. 395, Trease H, Friits J, Crowley W (eds). Springer: New York, 1991; 248–257.
4. Libersky LD, Petschek AG, Carney TC, Hipp JR, Allahdadi FA. High strain Lagrangian hydrodynamics: a three dimensional SPH code for dynamic material response. *Journal of Computational Physics* 1993; **109**:67–75.
5. Benz W, Asphaug E. Simulations of brittle solids using smooth particle hydrodynamics. *Computer Physics Communications* 1995; **87**:253–265.
6. Monaghan JJ. Simulating free surface flows with SPH. *Journal of Computational Physics* 1994; **110**:399–406.
7. Takeda H, Miyama SM, Sekiya M. Numerical simulation of viscous flow by smoothed particle hydrodynamics. *Progress of Theoretical Physics* 1994; **92**(5):939.
8. Morris JP, Fox PJ, Zhu Y. Modeling low Reynolds number flows using SPH. *Journal of Computational Physics* 1997; **136**:214–226.
9. Cummins SJ, Rudman M. A SPH projection method. *Journal of Computational Physics* 1999; **152**:584–607.
10. Shao S, Lo EYM. Incompressible SPH method for simulating Newtonian and non-Newtonian flows with a free surface. *Advanced Water Resources* 2003; **26**:787–800.
11. Clear PW, Monaghan JJ. Conducting modeling using smoothed particle hydrodynamics. *Journal of Computational Physics* 1999; **148**:227–266.
12. Monaghan JJ, Kocharyan A. SPH simulation of multi-phase flow. *Computer Physics Communications* 1995; **87**:225.
13. Monaghan JJ. Implicit SPH drag and dusty gas dynamics. *Journal of Computational Physics* 1997; **138**:801–820.
14. Morris JP. Simulating surface tension with smoothed particle hydrodynamics. *International Journal for Numerical Methods in Fluids* 2000; **33**:333–353.
15. Gutfraind R, Savage SB. Flow of fracture ice through wedge-shaped channels: smoothed particle hydrodynamics and discrete-element simulations. *Mechanics of Materials* 1998; **28**:1–17.
16. Cleary PW, Prakash M. Discrete-element modeling and smoothed particles hydrodynamics: potential in the environmental science. *Philosophical Transactions of Royal Society of London*, *Series A* 2004; **362**:2003–2030.
17. Monaghan JJ. SPH compressible turbulence. *Monthly Notices of the Royal Astronomical Society* 2002; **353**:25–39.
18. Maeda K, Sakai M. Development of seepage failure analysis procedure of granular ground with smoothed particle hydrodynamics (SPH) method. *Journal of Applied Mechanics* (JSCE) 2004; **7**:775–786 (in Japanese).
19. Liu GR, Liu MB. *Smoothed Particle Hydrodynamics*: *A Meshfree Particle Method*. World Scientific: Singapore, 2004.
20. Monaghan JJ. Smoothed particle hydrodynamics. *Report Progress in Physics* 2005; **68**:1703–1759.
21. Swegle JW, Hicks DL, Attaway SW. Smoothed particle hydrodynamics stability analysis. *Journal of Computational Physics* 1995; **116**(1):123–134.
22. Monaghan JJ. SPH without a tensile instability. *Journal of Computational Physics* 2000; **159**:290–311.
23. Gray JP, Monaghan JJ, Swift RP. SPH elastic dynamics. *Computer Methods in Applied Mechanics and Engineering* 2001; **190**:6641–6662.
24. Chen WF, Mizuno E. *Nonlinear Analysis in Soil Mechanics*: *Theory and Implementation*. Elsevier: Amsterdam, 1990.
25. Monaghan JJ, Lattanzio JC. A refined particle method for astrophysical problems. *Astronomic and Astrophysics* 1985; **149**:135.
26. Monaghan JJ. Smoothed particle hydrodynamics. *Annual Review of Astronomy and Astrophysics* 1992; **30**: 543–574.

DOI: 10.1002/nag

27. Flammer I, Blum A, Leiser A, Germann P. Acoustic assessment of flow patterns in unsaturated soil. *Journal of Applied Geophysics* 2001; **46**(2):115–128.
28. Francesco A, Gregorio A, Filippo A, Nicola G. An acoustic method for soil moisture measurement. *IEEE Transactions on Instrumentation and Measurement* 2004; **53**:891–898.
29. Morris JP, Monaghan JJ. A switch to reduce viscosity. *Journal of Computational Physics* 1997; **136**:41–50.
30. Dyka CT, Randles PW, Ingel RP. An approach for tension instability in smoothed particle hydrodynamics (SPH). *Computers and Structures* 1995; **57**:573–580.
31. Dyka CT, Randles PW. Stress points for tension instability in SPH. *International Journal for Numerical Methods in Engineering* 1997; **40**:2325–2341.
32. Johnson GR, Beissel SR. Normalized smoothing functions for SPH impact computations. *International Journal for Numerical Methods in Engineering* 1996; **39**:2725–2741.
33. Morris JP. Analysis of SPH with applications. *Ph.D. Thesis*, Mathematics Department, Monash University, Melbourne, Australia, 1996.
34. Chen JK, Beraun JE, Carney TC. A corrective smoothed particle method for boundary value problems in heat conduction. *International Journal for Numerical Methods in Engineering* 1999; **46**:231–252.
35. Randles PW, Libersky LD. Normalized SPH with stress points. *International Journal for Numerical Methods in Engineering* 2000; **48**:1445–1462.
36. Fangming J, Monica SA. Oliveira, Antonio CMS. SPH simulation of transition to turbulence for planar shear flow subjected to a streamwise magnetic field. *Journal of Computational Physics* 2006; **217**:485–501.
37. Randles PW, Libersky LD. Smoothed particle hydrodynamics: some recent improvements and applications. *Computer Methods in Applied Mechanics and Engineering* 1996; **139**(1–4):375.

DOI: 10.1002/nag